

Bidirectional microwave-optical conversion using an integrated barium-titanate transducer

Charles Möhl,^{1,2,*} Annina Riedhauser,^{1,3,*} Max Glantschnig,¹ Daniele Caimi,¹ Ute Drechsler,¹ Antonis Olziersky,¹ Deividas Sabonis,¹ David Indolese,¹ Thomas Karg,^{1,†} and Paul Seidler^{1,‡}

¹IBM Research Europe, Zurich, Säumerstrasse 4, Rüschlikon, CH-8803 Switzerland

²Department of Physics, ETH Zürich, Zurich, CH-8093 Switzerland

³Institute of Physics, EPF Lausanne, Lausanne, CH-1015 Switzerland

Efficient, low-noise, high-bandwidth transduction between optical and microwave photons is key to long-range quantum communication between distant superconducting quantum processors. Recent demonstrations of microwave-optical transduction using the broadband direct electro-optic (Pockels) effect in optical thin films made of AlN or LiNbO₃ have shown promise. Due to the quadratic scaling of transduction efficiency with the electro-optic coefficient, material classes with stronger Pockels effects, such as the perovskite titanates BaTiO₃ or SrTiO₃, may unlock new performance regimes for future transducers. However, these materials require adapted designs and fabrication approaches due to their nonlinear and, in some cases, hysteretic electro-optic response, as well as limited process compatibility. Here, we engineer an on-chip, triply resonant transducer comprising low-loss BaTiO₃-on-SiO₂ waveguides monolithically integrated with a superconducting microwave resonator made of Nb. Exploiting the bias-induced Pockels effect of BaTiO₃, we demonstrate bidirectional microwave-optical transduction at millikelvin temperatures and total off-chip efficiencies reaching 1×10^{-6} in pulsed operation. We establish a device concept permitting in-situ poling of the ferroelectric material without introducing excess microwave loss and tuning of the optical system without sacrificing microwave-optical overlap. Using a fully subtractive process, we fabricate Nb air bridges for crossings of conductors and both air- and oxide-clad optical waveguides. We investigate optically-induced heating through pulsed optical pumping, revealing fast thermalization and quasiparticle resilience of the microwave resonator. Our transducer concept is applicable to other materials with a large bias-induced Pockels effect and paves the way for efficient, low-power quantum interconnects.

I. INTRODUCTION

Quantum computing promises to revolutionize many areas across academia and industry [1]. Because of their long coherence times, fast gates, and scalability, on-chip superconducting qubits represent a front runner for universal quantum computation [2]. Beyond scaling to larger numbers of qubits in order to achieve practical quantum advantage, additional functionality may be provided by the ability to send and receive quantum information between distant quantum computing units, allowing them to be interconnected in a quantum network. However, operating at frequencies of ~ 5 GHz, superconducting qubits must be cooled to temperatures of ~ 10 mK in order to suppress thermal decoherence and ensure high-fidelity computation. Despite efforts to create cryogenically cooled, low-loss, microwave quantum links [3] for modular systems, an entire system maintained at millikelvin temperatures is not a viable solution for long-range interconnects between quantum processing units.

Optical photons on the other hand offer negligible thermal noise, high bandwidth, and orders-of-magnitude lower propagation losses at room temperature, using either fiber [4, 5] or free-space transmission [6, 7]. Optical quantum systems have thus been employed to pioneer entanglement distribution over hundreds of kilometers [4, 5, 8–10], paving the way towards a quantum internet [11, 12]. Recently, demonstrations of efficient, low-noise, microwave-optical photon interconversion

[13, 14] have sparked the idea of networking superconducting quantum systems by means of optical quantum communication [15]. Central to reaching this goal is a quantum transducer capable of entangling microwave and optical photons with high fidelity and large bandwidth.

Currently, the most advanced approaches to an integrated quantum transducer are piezo-opto-mechanical [16–21] and direct electro-optic [22–25] systems. Whereas the former relies on an intermediary mechanical resonance serving as an interface to both microwave and optical modes, the latter directly couples microwave and optical photons via the Pockels effect. Classically, direct electro-optic coupling can be described as a modulation of the optical refractive index proportional to the Pockels coefficient r and an applied microwave field E . The direct electro-optic approach is appealing because it avoids the complexity and potential added noise of an intermediary mode. In bulk devices, electro-optic transduction has been demonstrated with efficiency close to unity and added noise below one photon [26]. First proof-of-concept demonstrations have shown microwave-optical entanglement [27] as well as optical control [25] and readout of a superconducting qubit [28]. In addition to scalability and higher efficiency for a given pump power, integrated devices offer the prospect of GHz bandwidths [29].

Following initial demonstrations using aluminum nitride (AlN, $r = 1$ pm/V) [22, 30], most transducer devices today employ optical waveguides made of the ferroelectric lithium niobate (LiNbO₃, $r = 30$ pm/V) [23–25, 31, 32] (Fig. 1a). The primary route to improving efficiency has so far been the enhancement of the optical quality factor, with internal quality factors recently reaching 2.9×10^7 (1.93×10^8) in optimized integrated [33] (bulk [34]) devices. Although the transduc-

* The authors contributed equally to this work.

† Contact author: thomas.karg@ibm.com

‡ Contact author: pfs@zurich.ibm.com

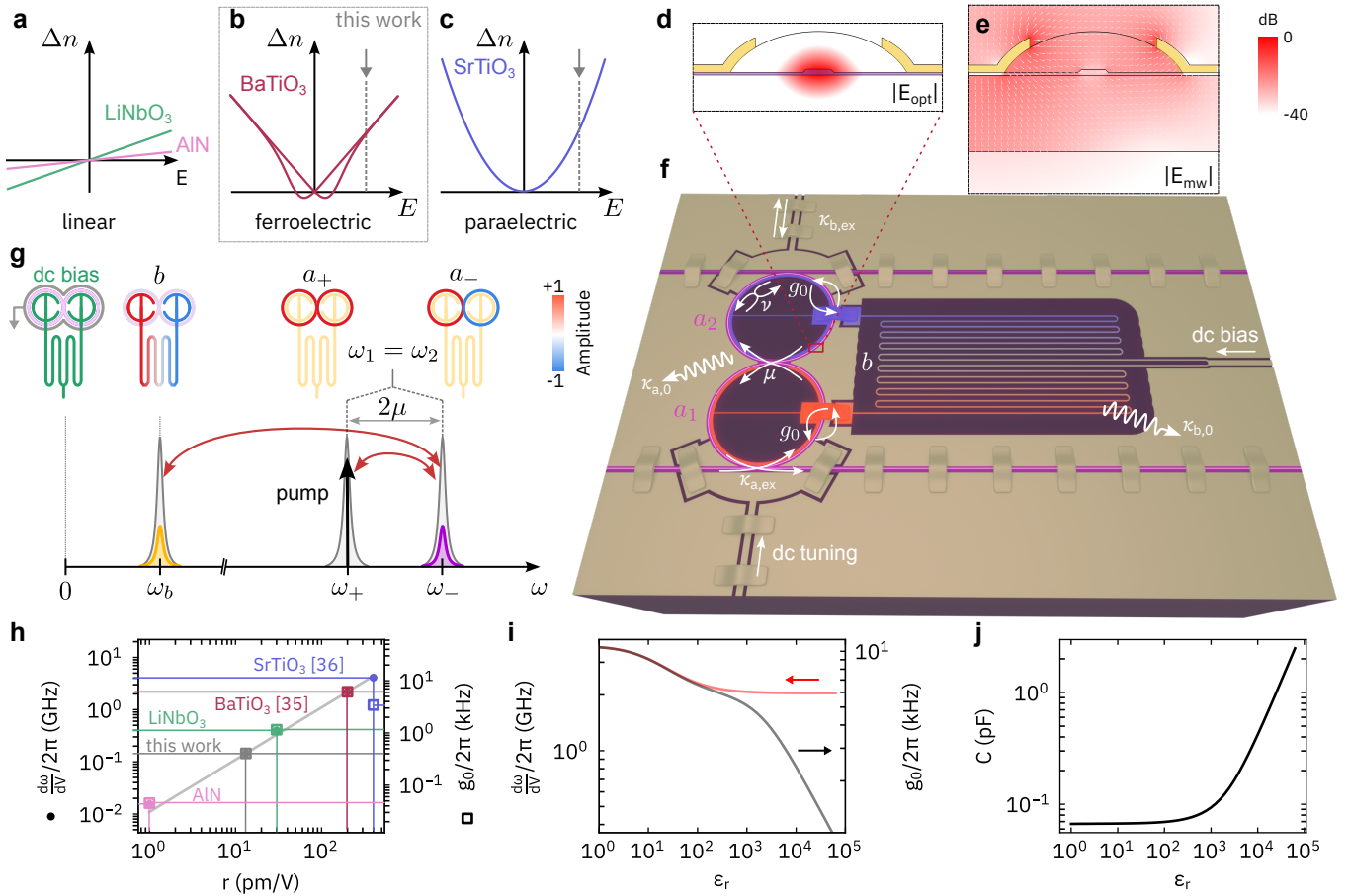


Figure 1. Electro-optic transducer design for materials with nonlinear Pockels effect. (a-c) Diagrams of refractive index change Δn vs. applied dc electric field E for (a) linear electro-optic materials AlN, LiNbO₃, and non-linear electro-optic materials: ferroelectric BaTiO₃ (b), and SrTiO₃ in the quantum paraelectric phase (c). Grey arrows and dashed lines in (b) and (c) indicate working points at non-zero bias fields. (d,e) Simulated optical and microwave field amplitudes, respectively, in a cross section of BaTiO₃ ridge waveguide and superconducting electrodes. (f) Schematic of the integrated, triply resonant transducer consisting of a photonic molecule formed by two evanescently coupled optical ring resonators (a_1, a_2) and a $\lambda/2$ -type microwave resonator (b). A voltage applied at the dc bias port poles the electro-optic material, and a voltage at the dc tuning port tunes the two ring resonators into resonance. (g) Scattering picture of triply resonant microwave-optical transduction. The hybridized photonic molecule modes a_{\pm} produce an antisymmetric beating that is phase-matched to the microwave field distribution b . Pumping on the lower optical resonance coherently scatters photons between b and a_{-} when the microwave resonance frequency ω_b matches the optical splitting 2μ . Shown is also the symmetric dc bias field poling the material. (h) Simulation of electro-optic frequency pulling factor $\partial\omega_a/\partial V$ (circles) and single-photon coupling strength g_0 (rectangles) as a function of the Pockels coefficient r for different materials. (i) Simulated $\partial\omega_a/\partial V$ (red) and g_0 (black) for $r = 200$ pm/V as function of ϵ_r . (j) Total microwave resonator capacitance as function of ϵ_r . For (i) and (j) $\omega_b/2\pi = 6.8$ GHz is kept constant.

tion efficiency scales quadratically with loaded optical quality factor Q_a , this gain comes at the cost of reduced optical bandwidth. If a transduction bandwidth of ~ 10 MHz is to be maintained, Q_a is limited to about $\sim 2 \times 10^7$ at an optical vacuum wavelength of 1550 nm. Beyond this point, an increase of the internal quality factor $Q_{a,0}$ improves efficiency only linearly, and only if either mode-selective coupling is implemented or the fiber-chip coupling losses are negligibly small, both of which lead to additional device complexity. Hence, further advances using established materials, especially in integrated devices, will be challenging and lead to increasingly difficult trade-offs between reliability, manufacturability, device footprint, bandwidth, and added noise.

There is therefore increasing interest in integrating alterna-

tive materials with larger electro-optic coefficients, enabling more efficient transducers operating at lower optical pump intensities. Promising candidates are the perovskites barium titanate (BaTiO₃) and strontium titanate (SrTiO₃). For BaTiO₃, effective Pockels coefficients of $r = 500$ pm/V and 200 pm/V have been reported in thin films at 300 K and 4 K, respectively [35], while for SrTiO₃, values of up to $r = 400$ pm/V were demonstrated in a bulk device at 4 K [36]. Whereas single-crystalline LiNbO₃, with its high Curie temperature over 1300 K [37], features a permanent polarization, stable ferroelectric phase and a linear electro-optic response in the temperature range of interest for quantum applications (10 mK - 300 K) (Fig. 1a), the large electro-optic response of BaTiO₃ and SrTiO₃ stems from operation in the vicinity of

phase transitions, usually marked by a divergence in permittivity. Indeed, the Curie temperature of BaTiO₃ is 420 K [38], and a phase transition occurs at around 240 K, accompanied by a peak in the electro-optic response ($r \approx 700$ pm/V) [35]. In BaTiO₃, the Pockels effect is hysteretic due to ferroelectric domain poling (Fig. 1b), and maximizing the electro-optic response of BaTiO₃ requires a static electrical bias field to orient the domains [39]. In contrast, the Curie temperature of SrTiO₃ is close to 0 K, giving rise to a quantum paraelectric phase near this temperature [40] and, in turn, a large quadratic electro-optic response [36, 41] (Fig. 1c). Thus, both BaTiO₃ in its ferroelectric phase (Fig. 1b) and SrTiO₃ in its quantum-paraelectric phase (Fig. 1c) exhibit nonlinear electro-optic responses requiring a dc-bias field to control and harness the effect for applications such as quantum transduction.

Despite the promising electro-optic properties of materials like BaTiO₃ and SrTiO₃, their use in integrated devices faces several challenges: i) There are no commercially available (single-)crystalline thin films with the necessary optical quality. ii) The material properties depend on growth parameters, film thickness, strain, temperature and environmental conditions, such as the presence of oxygen or water vapor [39, 42]. iii) An electrical circuit designed for dc-biasing of the active material is required.

Here, we take a first step to address these challenges by developing the design and fabrication processes for an integrated triply resonant electro-optic transducer employing nonlinear electro-optic materials. The transducer is capable of in-situ poling without incurring microwave losses, as well as independent tuning of the photonic resonances without sacrificing electro-optic mode overlap. Using a device fabricated with BaTiO₃, we show bidirectional continuous-wave (cw) and pulsed transduction with efficiency that scales linearly up to peak in-fiber optical pump powers of 12 dBm. Further, we investigate optically induced heating of the microwave circuit. Due to their different dynamics, we can distinguish fast in-cavity dielectric heating and slower substrate heating, as well as quasiparticle effects. We find that in-cavity heating dominates over the other mechanisms at optical pump powers relevant for quantum transduction.

II. TRANSDUCER DESIGN

Our on-chip transducer consists of a photonic molecule integrated with a quasi-lumped-element superconducting microwave resonator (Fig. 1f). Two optical ring resonators comprising ridge waveguides (Fig. 1d) are coupled evanescently at rate μ to form the photonic molecule [23–25, 31, 32]. In the case of rings with resonant modes, the respective modes a_1 and a_2 hybridize into symmetric and antisymmetric normal modes $a_{\pm} = (a_1 \pm a_2)/\sqrt{2}$ with frequencies ω_{\pm} , respectively (Fig. 1g). The microwave resonator is composed of two capacitors enclosing the optical waveguides (Fig. 1e) and a connecting meandered inductor and is dimensioned to have a half-wavelength ($\lambda/2$) microwave field distribution (mode b) matching the antisymmetric optical beating $a_+^\dagger a_- + a_-^\dagger a_+$. For triply resonant frequency conversion, we

match the photonic molecule splitting to the microwave resonance frequency ω_b , *i.e.*, $\omega_- - \omega_+ = 2\mu = \omega_b$.

The optical rings are tuned into resonance with a voltage applied at the dc-tuning port. By connecting the bias port to the microwave resonator at its voltage node, we avoid incurring excess microwave loss. Using an additional dc-bias port, the electro-optic material comprising the optical waveguides can be poled to induce a linear Pockels effect. For input and output, an optical bus waveguide couples to the lower ring resonator and a microwave coplanar waveguide capacitively couples to the microwave resonator at the top.

The electro-optic interaction in our device is described by the Hamiltonian $H_{\text{int}} = \hbar g_0 (a_+^\dagger a_- + a_-^\dagger a_+) (b + b^\dagger)$ with vacuum electro-optic coupling constant $g_0 = G V_{\text{zpf}}$. Here, $G = \partial\omega_a/\partial V$ is the frequency pulling factor and $V_{\text{zpf}} = \sqrt{\hbar\omega_b/2C}$ is the microwave resonator's zero-point voltage. Critical parameters determining the strength of g_0 are the Pockels coefficient r and the relative permittivity ϵ_r of the electro-optic material, the microwave-optical mode overlap, and the effective transducer capacitance C (see App. A).

We can estimate g_0 via numerical simulations. We first derive an equivalent circuit for the microwave resonator that is motivated by the $\lambda/2$ field distribution obtained from a fully three-dimensional (3d) finite-element simulation (Sec. A 4 and Fig. 7). This breaks down the problem into simulations of individual capacitances and inductances. We can then determine the effective capacitance of the transduction electrodes and electro-optic mode overlap as a function of the relative permittivity ϵ_r . Exploiting angular symmetry, the overlap integral is performed on a two-dimensional cross-section of the optical waveguide and transduction electrodes (Fig. 1d,e).

We thus compute g_0 and G as a function of r for different electro-optic materials (Fig. 1h). The simulation predicts $g_0/2\pi = 0.05$ kHz for AlN [43], $g_0/2\pi = 1.2$ kHz for LiNbO₃ ($r = 30$ pm/V, $\epsilon_r = 25$) [43], and $g_0/2\pi = 6.1$ kHz for BaTiO₃ ($r = 200$ pm/V, $\epsilon_r = 200$ [35]). For quantum paraelectric SrTiO₃, a value of $g_0/2\pi \approx 3.4$ kHz is obtained assuming the currently highest reported value of r in a bulk device ($r = 400$ pm/V, $\epsilon_r = 2 \times 10^4$) [36]. Assuming perfectly quadratic behavior, the much smaller electrode gap and therefore larger achievable bias fields in integrated devices may enable significantly larger values of r and g_0 . The value of g_0 for LiNbO₃ is comparable to other published devices [23–25, 31]. As expected, there is an approximate linear relationship between g_0 or G and r (solid line in Fig. 1h computed with $\epsilon_r = 200$). Deviations from the linear relation are caused by the vastly different material permittivities, in particular that of SrTiO₃. Large permittivity reduces the electro-optic mode overlap by suppressing the microwave field penetration of the optical ridge waveguide and increases the transducer capacitance.

To elucidate the dependence on relative permittivity ϵ_r , we simulate g_0 and G as a function of ϵ_r between 1 and 10^5 for $r = 200$ pm/V (Fig. 1i). The microwave resonance frequency is kept constant by adapting the inductance. At low $\epsilon_r \approx 1$, the field penetrates the waveguide core both directly through the slab in contact with the electrodes and through the optical cladding ($\epsilon_{r,\text{SiO}_2} \approx 4$). With increasing permittivity,

the field penetration through the cladding becomes insignificant and plays virtually no role for permittivities above 10^2 (Fig. 1i), where the field strength in the waveguide core saturates to half of that in the slab, roughly corresponding to the ratio of the slab and total waveguide thicknesses. This means that G and g_0 reduce by the same amount and reach a plateau at large $\epsilon_r \sim 10^2$ (Fig. 1i), a fact that should be considered in waveguide optimization. For even larger ϵ_r exceeding 2×10^3 we see another drop in g_0 caused by the increase of transducer capacitance (Fig. 1j). In this regime the capacitance of the transduction electrodes dominates over the stray capacitance and lowers V_{zpf} . This effect can be mitigated to some extent by making the device smaller.

Our simulations show that this transducer design can achieve large vacuum electro-optic coupling strengths in the kHz range with LiNbO₃, BaTiO₃ or SrTiO₃. Despite the large permittivities of these materials, strong microwave-optical overlap is maintained by the use of a ridge waveguide with low ridge-slab contrast and electrodes in direct contact with the slab.

III. DEVICE IMPLEMENTATION

Our transducer device (Fig. 2a) is fabricated in a fully subtractive process (see Sec. C 1). Optical ridge waveguides are defined by dry-etching of a 225-nm BaTiO₃ film bonded to an oxidized Si substrate and are later cladded with SiO₂. The microwave circuit is made entirely of Nb. The fabrication process differs from that of other transducer realizations [22–25, 30–32] in several important respects: lithographically defined superconducting air bridges are employed for optical and electrical circuit crossings; the microwave circuit includes a symmetry-preserving dc-bias port for poling in addition to the dc-tuning port for frequency-matching; and a large electrode coverage of the ring resonators of 91% is achieved.

The air bridges enable optical waveguide-superconductor and superconductor-superconductor crossings for complex layouts. The process preserves sub-micron critical dimensions, *e.g.*, for nanowire inductors in the main metallization layer. They are compatible with both oxide-clad (Fig. 2c) as well as air-clad optical waveguides (Fig. 2d). Note that air bridges are included in the current-carrying portion of the microwave resonator connecting the inductor with the transduction electrodes. This is an advancement over the typical use of air bridges as patches between regions of the ground plane, through which no significant current flows. A waveguide cross section (Fig. 2b) showcases the dome-shaped cladding that enables a clean subtractive electrode fabrication instead of a lift-off, allowing thicker superconducting films. Without the dome shape, the sputter-deposited Nb layer would not be cleared cleanly from any vertical sidewall during dry-etching, risking the creation of a short-circuit.

To pole the BaTiO₃ and produce a net non-zero Pockels effect, a dc bias line is galvanically connected to the inductor at its midpoint. Microwave leakage through this port is thus minimized by making the microwave design, and thus the microwave mode distribution, symmetric about a line bisecting

the entire transducer layout. The symmetry of the layout is further maintained by having two optical bus waveguides pass along the upper and lower ring resonators. While the lower bus waveguide is designed for critical optical coupling, the upper one is displaced a few microns from the upper ring resonator to avoid optical coupling. Instead, it couples to another device on the chip.

To tune the photonic molecule into resonance, a voltage can be applied at the dc-tuning electrode capacitively coupled to the transducer electrode of the lower ring resonator, instead of tuning with respect to ground, as is the case in all previous demonstrations. This means that the tuning sections are also part of the microwave resonator and contribute to transduction, resulting in a record-high usable electrode coverage of 91%. The tuning electrode as well as the microwave port electrode on the opposite side of the transducer are purposely wide to ensure a large external coupling rate $\kappa_{b,ex}$ through the microwave port electrode to the microwave bus.

The BaTiO₃ optical bus waveguides lead to the chip facets, which are defined by dry etching deep trenches into the Si substrate. Approaching the facet, the ridge waveguide is tapered to achieve good mode matching with an ultra-high-numerical-aperture (UHNA) optical fiber (Sec. C 2). Broadband optical fiber-to-chip coupling is achieved, as evidenced by the envelope of the optical transmission spectrum in Fig. 2e, in contrast to the comparatively narrowband grating couplers used in most transducer demonstrations to date [23–25].

The chip is packaged for cryogenic measurements by aligning UHNA fibers and gluing them to the chip (Sec. C 2). Wirebonding the chip to a microwave printed-circuit board and enclosing the assembly inside a copper cavity completes the packaging. During sample handling before mounting in the dilution fridge, one of the two optical fiber connections to the chip broke accidentally. Consequently, the transducer could only be probed optically in reflection. The reflected signal originates from moderate coherent back-scattering in the ring resonators. We initially characterize the optical transmission spectrum (Fig. 2e) at room temperature. Without bias or tuning voltages applied, a series of resonances of the lower ring resonator coupled to the optical bus waveguide are observed with a free-spectral range of 218 GHz (see Appendix E for further optical characterization). Monitoring the spectrum of a selected resonance at 1603.5 nm as a function of tuning voltage (Fig. 2f), we observe an avoided crossing between modes of the two ring resonators. The coherent coupling rate of the photonic molecule is thus determined to be $2\mu = 2\pi \times 4.7$ GHz. Because this value of μ is the largest observed and the closest to the microwave resonance frequency, this pair of coupled optical resonances is selected for transduction measurements.

The packaged transducer is cooled in a dilution refrigerator to a base temperature of 8 mK without any voltage applied to the device. The microwave resonance is then probed in reflection (Fig. 2g), at a bias voltage of -100 V, revealing the critically coupled transducer resonance at $\omega_b = 2\pi \times 6.82$ GHz, close to the simulated value. A spurious mode at 6.78 GHz is also detected, whose frequency does not tune with temperature and might originate from the package (see Appendix F for

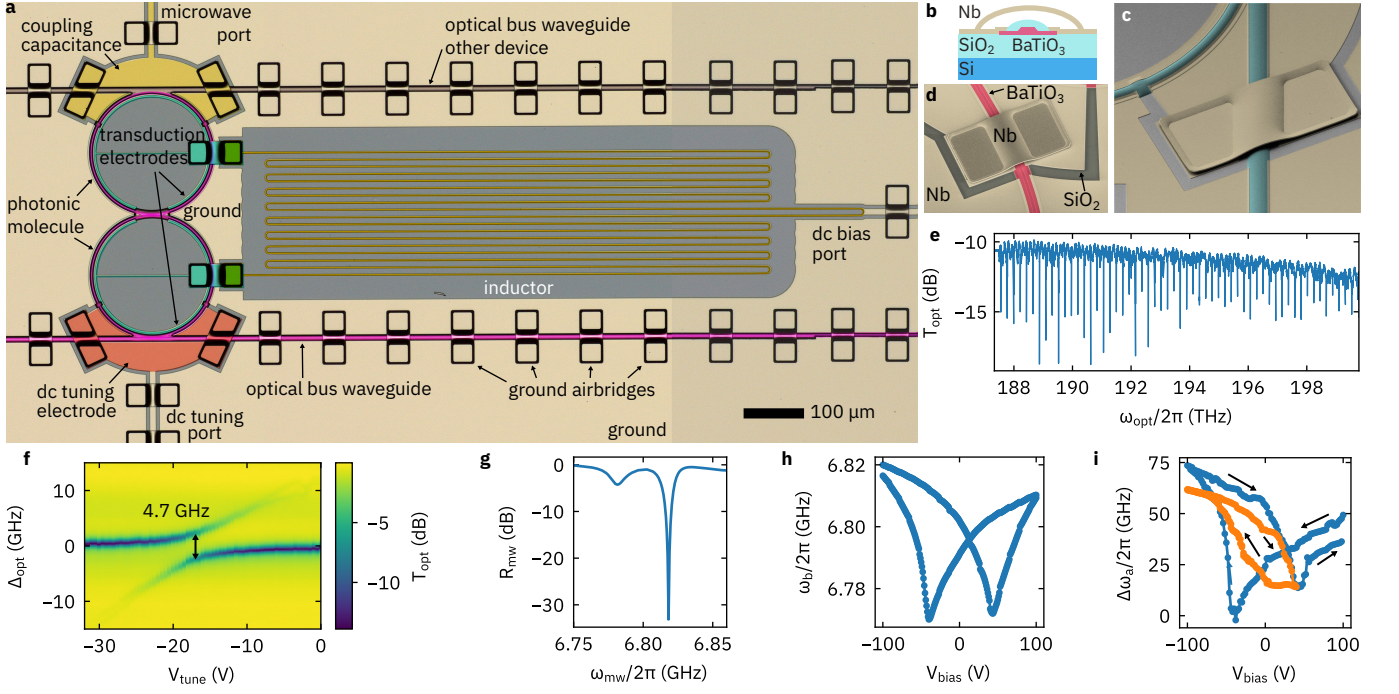


Figure 2. DC-biased triply resonant photonic molecule transducer. (a) False-colored optical micrograph of the photonic molecule transducer. Optical signals are evanescently coupled from the optical bus waveguide to the lower ring of the photonic molecule, which is evanescently coupled to the upper ring at its opposite side. Symmetric electrodes for dc-tuning (orange) of the photonic molecule and microwave bus coupling (yellow) are placed on each ring. (b) Schematic cross-section of the measured device, showing BaTiO₃ ridge waveguides on SiO₂ on Si and SiO₂ cladding. Nb electrodes are in contact with the BaTiO₃ slab, with Nb air bridges across, where required. (c) False-colored SEM micrograph of a representative Nb air bridge used throughout the design. (d) For illustration, an air bridge across an air-clad waveguide on another fabricated chip is shown. (e) Optical spectrum with a free-spectral range of 218 GHz measured in transmission at room temperature after optical packaging. (f) Optical avoided crossing as a function of dc-tuning voltage showing photonic molecule hybridization with a ring-ring coupling of $2\mu = 4.7$ GHz. (g) Microwave reflection measured at 10 mK at $V_{\text{bias}} = -100$ V revealing the microwave resonance at 6.82 GHz. (h) Tuning curve of the microwave resonance frequency as a function of dc-bias voltage showing ferroelectric hysteresis (arrows indicate tuning direction). (i) Tuning curve of the optical resonance measured in reflection at 75 mK. The blue data points show the initial hysteresis curve after cooldown which includes a drift due to material conditioning (open curve at +100 V). The orange data points show hysteresis when ramping the bias between $V_{\text{bias}} = -100$ V and $V_{\text{bias}} = +40$ V, corresponding to the coercive field.

more detailed microwave characterization). At low power, we find an internal microwave linewidth of $\kappa_{b,0} = 2\pi \times 10$ MHz ($Q_{b,0} = 7.0 \times 10^2$), limited by dielectric loss in the SiO₂ layer, and an external coupling rate of $\kappa_{b,\text{ex}} = 2\pi \times 7.2$ MHz ($Q_{b,\text{ex}} = 9.5 \times 10^2$) for coupling to the microwave feedline.

Ramping the bias voltage from -100 V to 100 V and back (Fig. 2h), we observe tuning of the microwave resonance due to the change of permittivity with applied field, with pronounced hysteresis due to the ferroelectricity of BaTiO₃. We observe similar hysteretic tuning for the optical resonance (Fig. 2i), albeit with more noise due to the measurement being made in reflection, which precludes an unambiguous assignment of the resonance frequency because of interference effects (Sec. F3). The initially recorded optical tuning curve cycling between 100 V and -100 V also exhibits drift, as this measurement was taken immediately after cooldown. The partial tuning curve cycling between -100 V and +40 V, the latter voltage corresponding to the coercive field at which ferroelectric domains are reoriented, shows a weaker hysteresis. For transduction measurements, the device was biased at -100 V, where the ferroelectric domains are maximally ori-

ented, achieving the strongest Pockels effect [39].

IV. BI-DIRECTIONAL CONTINUOUS-WAVE TRANSDUCTION

Having characterized the optical and microwave resonances individually, we set out to measure microwave-optical transduction. For these experiments, the device is poled at a bias voltage of -100 V. Without a possibility to directly measure the photonic-molecule splitting $\omega_b = 2\mu$ via optical spectroscopy at mK temperatures, the splitting was adjusted indirectly by optimizing the transduction efficiency as function of dc-tuning voltage (Sec. G).

For microwave-to-optical transduction (Fig. 3a), we apply a microwave modulation field b_{in} with frequency ω_{mw} close to ω_b at the microwave coupling port. The photonic molecule is pumped with a continuous-wave laser (frequency ω_p , power -11 dBm in fiber) near the resonance pair at 1603.5 nm. The electro-optic interaction drives both Stokes scattering $b \rightarrow a_{\pm}^{\dagger}$ to a photon with lower frequency $\omega_p - \omega_{\text{mw}}$ as well as anti-

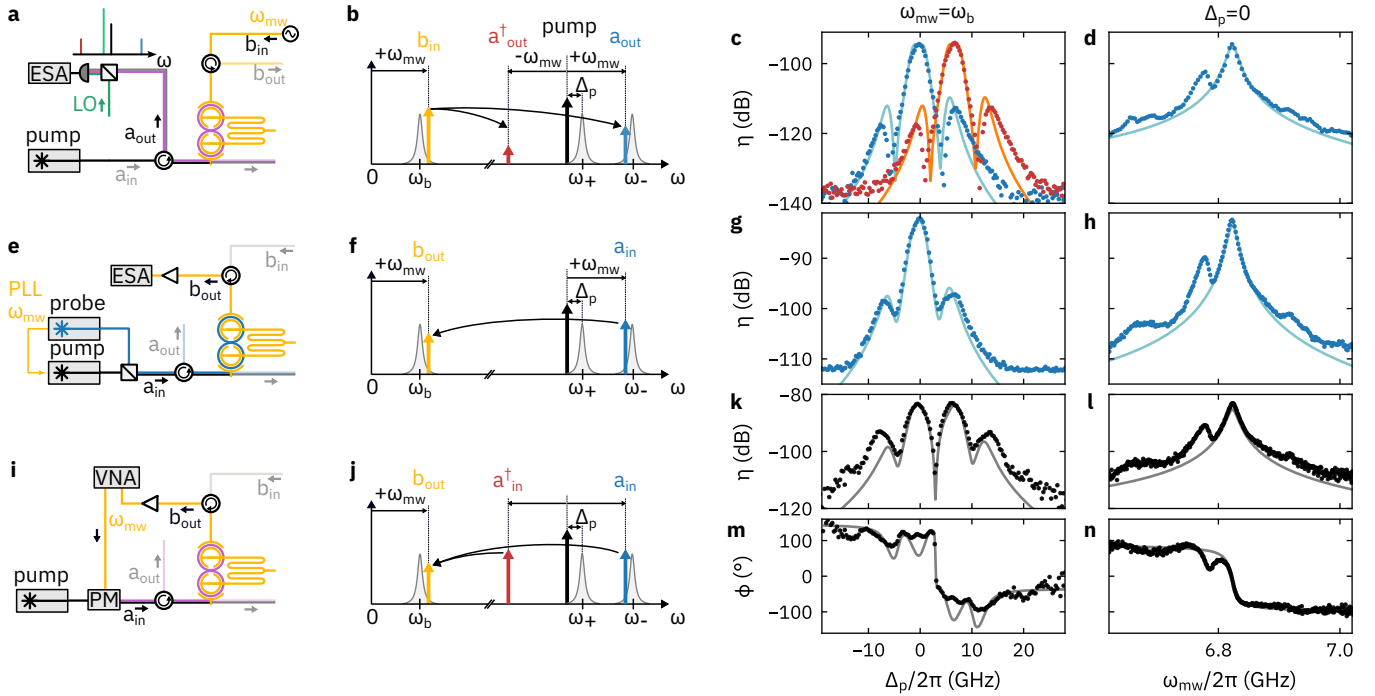


Figure 3. Bidirectional coherent triply resonant microwave-optical transduction. (a-d) Microwave-to-optical transduction. (a) Setup in which the transducer is driven by a microwave tone b_{in} and an optical pump. The optical signal a_{out} in backward direction is combined with a local oscillator (LO) and detected using heterodyne detection on an electronic spectrum analyzer (ESA). (b) Scattering diagram showing the microwave and optical resonances, the microwave tone (b_{in} , yellow), and the transduced optical Stokes (a_{out}^{\dagger} , red) and anti-Stokes (a_{out} , blue) sidebands. The optical pump is detuned by Δ_p from the lower photonic resonance ω_+ . (c) Transduction efficiency of the Stokes (red) and anti-Stokes (blue) processes on microwave-resonance ($\omega_{mw} = \omega_b$) as a function of Δ_p . (d) Transduction efficiency of a_{out} for optical pumping at $\Delta_p = 0$ as a function of ω_{mw} . (e-h) Single-sideband optical-to-microwave transduction. (e) Setup in which a blue-detuned probe laser is locked to the pump laser at a frequency offset ω_{mw} and both are driving the device at a_{in} . The transduced signal b_{out} is amplified and detected with on an ESA. (f) Scattering diagram showing probe laser photons a_{in} being scattered into the microwave mode at the laser offset frequency ω_{mw} . (g) and (h) show the transduction efficiency as a function of Δ_p and ω_{mw} , respectively. (i-n) Coherent optical-to-microwave transduction: (i) Setup in which a vector network analyzer (VNA) drives a phase modulator (PM) at frequency ω_{mw} , creating coherent sidebands on the pump laser driving the transducer at a_{in} . The transduced signal b_{out} is amplified and detected at the VNA. (j) The blue and red phase modulation sidebands are transduced simultaneously to the microwave mode. Both processes interfere because of the fixed phase relation between them. (k) and (l) show the efficiency and (m) and (n) the phase of the transduced signal as a function of Δ_p and phase-modulation frequency ω_{mw} , respectively. For all measurements, the optical pump power is -11 dBm in the fiber.

Stokes scattering $b \rightarrow a_{\pm}$ to a photon with higher frequency $\omega_p + \omega_{mw}$ (Fig. 3b). We detect the transduced photons emitted in the backward direction (a_{out}), *i.e.*, in reflection, using optical heterodyne detection, allowing us to distinguish both processes.

We first position the microwave tone on resonance $\omega_{mw} = \omega_b$ and measure the transduced optical signal as a function of optical pump detuning $\Delta_p = \omega_p - \omega_+$ (Fig. 3c). Normalizing the detected signals by the independently calibrated input powers, we extract the off-chip transduction efficiency η , including fiber-to-chip loss, which we estimate to be -5 dB from room-temperature characterization. The recorded efficiency curves for the Stokes and anti-Stokes processes are displaced in frequency with respect to each other by the photonic molecule splitting and reach a maximum around $\omega_p = \omega_-$ and $\omega_p = \omega_+$, respectively. The traces display the characteristic response of a triply resonant device. At the central peak, both optical pump and signal are resonant with respective modes of the photonic molecule. Two side peaks with lower amplitude

occur when only one of the optical pump and signal frequencies are resonant with an optical mode. These doubly-resonant side peaks are displaced from the triply resonant peak by the photonic molecule splitting ω_b .

Setting the pump laser to the lower photonic molecule resonance ($\Delta_p = 0$), we next measure transduction efficiency of the anti-Stokes sideband as a function of microwave frequency ω_{mw} (Fig. 3d). As expected, the data reveal the microwave resonance, including the previously observed spurious mode (Fig. 26). The transduction bandwidth is determined from the linewidth to be $\kappa_b = 2\pi \times 14$ MHz.

To measure the optical-to-microwave response of the system, we combine the optical pump with light from a blue-shifted probe laser that is phase-locked to the pump laser with a programmable frequency offset ω_{mw} (Fig. 3f). The light from both lasers is injected into the device in the forward direction (a_{in} , Fig. 3e). The transduced microwave signal is then amplified using a high-electron-mobility transistor (HEMT) and acquired using an electrical spectrum analyzer. Again,

we measure the transduction efficiency as a function of optical pump detuning, keeping the pump-probe offset fixed at $\omega_{\text{mw}} = \omega_b$ (Fig. 3g). The data show a triply resonant response similar to that of the microwave-to-optical experiment. However, the overall efficiency is more than 10 dB higher. We attribute this difference to the low backscattering efficiency in our device reducing the observed microwave-to-optical signal; the backscattering rate has no effect on the optical-to-microwave data. Fixing the optical pump signal at $\Delta_p = 0$, a sweep of the pump-probe frequency offset ω_{mw} again traces out the microwave resonance (Fig. 3h).

To understand the electro-optic response of the device, we model the transducer as a linear system and determine its electro-optic S-matrix (see Appendix B 3). We fit the data using model curves determined by the S-matrix coefficients (Fig. 3), varying fiber-chip loss, the photonic-molecule coupling strength μ , the ring-resonator detuning $\Delta_{\text{rr}} = \omega_1 - \omega_2$, as well as the coherent optical forward-backward coupling rates $\nu_{1,2}$. The optical and microwave loss rates are determined from independent spectroscopy (Fig. 2f,g) and the vacuum electro-optic coupling strength g_0 from electro-optic dc tuning (Sec. E 2). All system parameters are summarized in Tab. V of the appendix.

We find very good agreement between the fit curves and the data; the triply resonant response as well as the dips in between the doubly and triply resonant peaks are reproduced by the model. We find that the reduced microwave-to-optical transduction efficiency of the signal emitted in the backward direction is well explained by a low forward-backward coupling strength of $\nu_{1,2} \approx 0.1\kappa_a$. However, since neither the peaks at triple or double resonance are split (Fig. 31c,g), intra-ring forward-backward coupling cannot clearly be distinguished from residual backscattering that may occur, *e.g.*, at the end facet of the bus waveguide.

The measured bidirectional efficiencies are consistent with the vacuum electro-optic coupling rate of $g_0 = 2\pi \times 406$ Hz extracted independently from dc-tuning of the optical resonance frequency (see Appendix E 2). This corresponds to an effective material Pockels coefficient of only $r = 13$ pm/V, which is more than an order of magnitude lower than the value $r = 200$ pm/V previously reported for BaTiO₃ thin films at cryogenic temperatures [35] (Fig. 1h). Possible explanations include variations in material quality and processing but also a difference in strain in the BaTiO₃. Indeed, it has been reported that the electro-optic response in perovskite titanate films, and strong electro-optic materials in general, depends on strain [44]. This is confirmed by first-principles calculations for BaTiO₃ thin films [42] and it has also been shown to affect the phase diagram of SrTiO₃ [45]. Since those materials typically also feature large thermal expansion coefficients [44], strain engineering is likely going to be a key consideration for cryogenic applications.

Finally, we measure phase-coherent optical-to-microwave transduction using a vector network analyzer (VNA). An external phase modulator driven by the VNA creates blue and red sidebands at $\pm\omega_{\text{mw}}$ on the pump light injected into the device (Fig. 3i). As the two optical sidebands have a fixed phase relation, *i.e.*, $a_{\text{in}} \propto i(e^{-i\omega_{\text{mw}}t} + e^{i\omega_{\text{mw}}t})$, their simulta-

neous transduction leads to interference, which becomes apparent when sweeping Δ_p at fixed $\omega_{\text{mw}} = \omega_b$ (Fig. 3k). Now, two triply resonant peaks arise, with destructive interference occurring at a pump detuning symmetric with respect to the two photonic molecule modes due to the π -phase shift between the two phase-modulation sidebands, *i.e.*, $a_{\text{in}} = -a_{\text{in}}^\dagger$. In the phase response (Fig. 3m), a π phase shift at the point of symmetric detuning is also observed and well captured by the model. The smaller features, however, are exaggerated by the simulation, suggesting a slight deviation of the parameters from those of the actual device. When the pump is tuned to ω_+ ($\Delta_p = 0$), the microwave frequency dependence of the transduced signal (Fig. 3l) is dominated by the blue sideband, as the red sideband is far off resonance, and therefore looks virtually identical to the previous measurement (Fig. 3h). Additionally, the phase of the measured signal (Fig. 3n) agrees well with the predicted oscillator response, confirming that the process is coherent.

V. OPTICAL HEATING

We now investigate optical-pump-induced heating of the superconducting circuit, which is known to cause microwave decoherence, add noise, and limit the transduction efficiency. Tolerance to optical pumping is thus an important aspect of a quantum transducer.

There are two main pathways through which optical photons can contribute to heating of the microwave circuit (Fig. 4a): (i) straylight created by scattering at the fiber-chip interface irradiates the circuit, or (ii) light is coupled into the optical bus waveguide and, when resonant, to the photonic molecule where it is absorbed or scattered to the superconductor. Whereas straylight causes a near homogeneous irradiation of both the capacitors and the inductor, coupled resonant light is confined to the optical rings and predominantly affects the capacitors. Due to these distinct intensity distributions, straylight and coupled light result in different heating dynamics.

We probe the possible heating mechanisms using pulsed optical pumping. Laser pulses with a duration of 1 μs and a repetition rate of 1 kHz are generated by an acousto-optic modulator (AOM), amplified by an erbium-doped fiber amplifier (EDFA) and sent to the device (Fig. 4a). The in-fiber optical peak power P_{opt} is varied between 0 and 24 dBm.

The effects of stray-, coupled and in-cavity light are distinguished by controlling the optical detuning Δ_p and the fiber-chip coupling efficiency. To investigate straylight effects, we deliver light through the second, misaligned optical fiber such that no light is coupled to the on-chip waveguide (Fig. 4a). We further detune the light from any optical resonance. We note that the fiber-chip coupling point of this second fiber is located closer to the device than that of the primary fiber with good coupling efficiency. To study heating from in-cavity light, we couple light through the primary fiber and step the optical detuning across the resonances.

The response of the microwave resonator before, during, and after an optical pulse is probed using a microwave pulse synchronized to the optical pulse (Fig. 4b). Microwave spec-

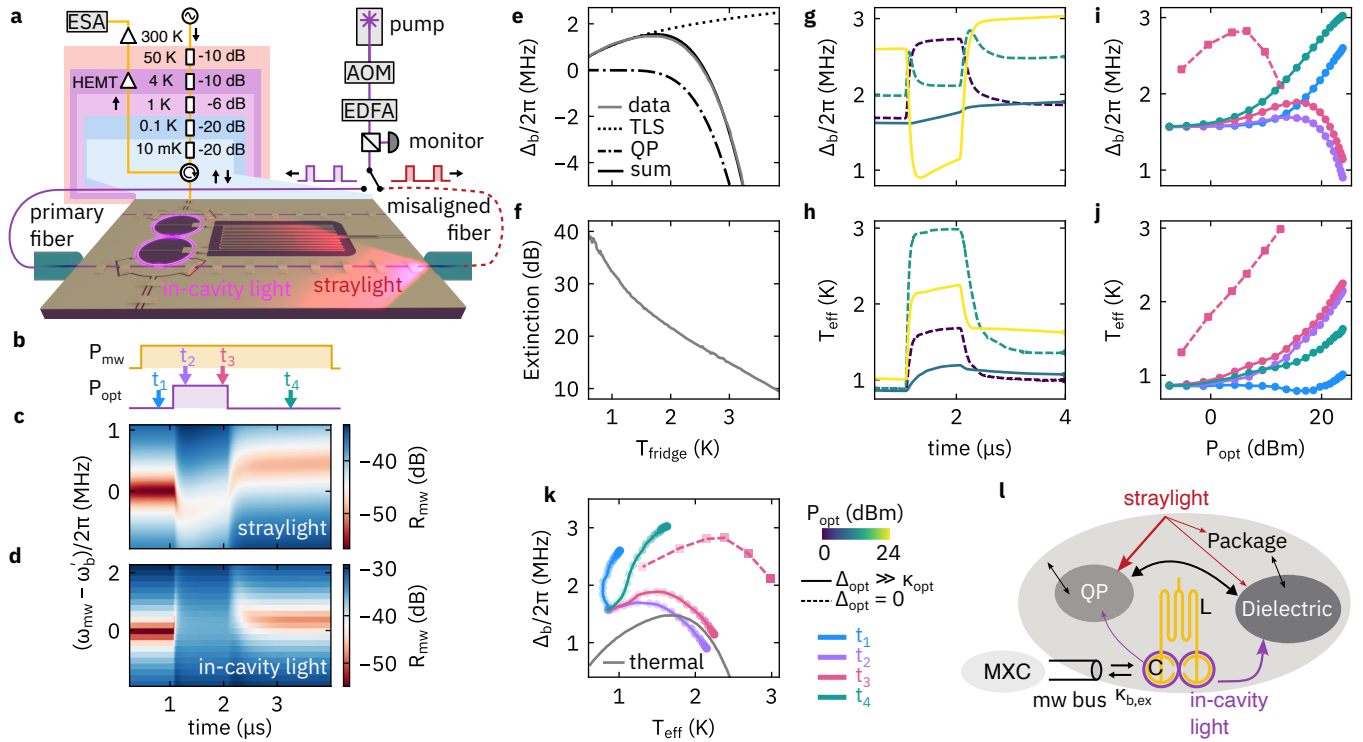


Figure 4. Microwave response under optical pump. (a) Experimental setup: A pump laser is pulsed using an acousto-optic modulator (AOM) and amplified with an erbium-doped fiber amplifier (EDFA). The pulse power is monitored using a fast photo diode and sent to the device either through the primary or misaligned optical fiber. Time-resolved microwave spectroscopy is performed using a pulsed high-power microwave source and an electronic spectrum analyzer (ESA). Light is guided to the chip either through the primary fiber with good coupling efficiency to the waveguide, or through the second, misaligned fiber, to study effects of in-cavity light or straylight, respectively. (b) Pulse sequence with the microwave pulse starting before and ending after the optical pulse. Colored arrows mark times at which microwave resonator properties for optical-power and detuning-dependent studies were evaluated. (c,d) Example raw time-resolved microwave spectra with (c) off-resonant straylight pulses via the misaligned fiber and (d) resonant, in-cavity light pulses via the primary fiber, using in-fiber optical powers of 18 and 19 dBm, respectively. During the optical pulse, a shift and reduced extinction of the microwave dip are clearly observed, which partially recovers after the pulse. (e) Microwave resonator frequency shift Δ_b as a function of cryostat temperature T_{fridge} without optical light. A theoretical model for Δ_b that is a sum of quasiparticle (QP) and two-level system (TLS) contributions is fit to the data. (f) Microwave resonator extinction ratio as a function of cryostat temperature used to calibrate effective temperature T_{eff} in optical heating experiments. (g) Frequency shift Δ_b and (h) effective temperature T_{eff} determined at each time during the pulse sequence. Different traces correspond to selected optical peak powers (colorbar) and off- (solid line) or on-resonant (dashed line) optical light. (i) Frequency shift Δ_b and (j) effective temperature T_{eff} as a function of optical peak power at different times in the pulse sequence (arrows in (b)). (k) Microwave frequency shift vs. effective temperature for optical and thermal experiments. (l) Diagram of heating mechanisms: The microwave mode is coupled to three baths: quasiparticles (QP), dielectric, and the mixing chamber (MXC) through the microwave bus. Optical straylight primarily heats the QP bath, while in-cavity light predominantly causes fast heating of the dielectric at the capacitor gap. Both QP and dielectric baths are thermalized to the chip package which itself is cooled by the MXC.

tra for straylight (Fig. 4c) and in-cavity light (Fig. 4d) both show a reduction in the resonant extinction and a red-shift versus a blue-shift, respectively, during the optical pulse. By fitting the spectra acquired at each time bin, we determine the evolution over time of the frequency shift and extinction of the resonance dip.

To translate the observed time dependence of the frequency shift and microwave resonator damping rate into a dependence on effective temperature, we separately measure the microwave response as a function of cryostat temperature (Fig. 4e,f). Interestingly, we observe an initial blue-shift with increasing temperature that turns into a red-shift for temperatures above 2 K (Fig. 4e, see Appendix F3 for details and extended range). While a red-shift is expected from Bardeen-

Cooper-Schrieffer (BCS) theory of quasiparticles in a superconductor ([46]), the blue-shift is unexpected. A blue-shift has been reported to originate from a temperature-dependent contribution to the dielectric constant from two-level systems (TLS) in the dielectric [47]. Here, it most likely stems from TLS in either the BaTiO_3 and/or the SiO_2 optical cladding in the transducer capacitor gap. We plot the fitted theory curves for both dielectric and BCS models (Fig. 4e) as well as the sum of the two, which is in good agreement with our data (Sec. F3). Due to the coupling to a spurious microwave mode (Sec. F1), a determination of the microwave quality factor would potentially be subject to systematic errors. Instead, we use the relationship between the measured extinction of the microwave resonance and the cryostat temperature T_{fridge}

(Fig. 4f) as a calibration for the effective temperature (T_{eff}) during optical pumping. While this effective temperature has no direct physical meaning, it is most likely dominated by quasiparticle-induced losses, as the TLS quality factor usually increases with temperature [48]. Therefore, T_{eff} should be close to the quasiparticle temperature, while the temperature of the dielectric may be different.

Figs. 4g and h show the measured frequency shift and effective temperature, respectively, as a function of time during pulsed optical pumping for resonant and off-resonant light as well as various optical powers. Off-resonant light at low power causes a blue shift and a weak temperature increase with a time constant $\sim 1 \mu\text{s}$. At high power, the temperature increase becomes much faster, following essentially the rise of the optical power ($\sim 0.1 \mu\text{s}$). The frequency now shifts strongly to the red starting from a blue-shifted background level. Resonant light causes a stronger temperature increase during the optical pulse with fast rise time, quasi instantaneously following the optical pulse shape. The frequency shift during the pulse is a strong blue-shift at lower powers. At high power, a red-shift with slightly lower rise time superimposes on the blue-shift, as seen by the peaks at the beginning and end of the optical pulse. All traces show a strong rise of the background temperature after the optical pulse (Fig. 4h), proportional to optical power, due to in-pulse heating which is slowly decaying to a steady-state (i.e. before pulse) at a rate of $\sim 10 \text{ kHz}$ (Appendix H) by thermalization with the substrate. The background frequency shift also increases with optical power (Fig. 4g), but the difference between levels after and before the pulse is less pronounced. Part of the background level is caused by output noise of the EDFA (average power -22 dBm).

Using the thermal model, we identify dielectric and quasiparticle heating with blue and red frequency shifts, respectively. This implies that straylight alone causes primarily slow heating of the substrate and dielectric, resulting in a weak temperature increase. In addition, fast quasiparticle heating (red-shift) is induced by photons hitting the inductor. Resonant in-cavity light, however, predominantly causes dielectric heating as indicated by the strong blue-shift. The much faster fall- and rise-time (even slightly faster than quasiparticle dynamics) may be explained by its confinement to the ring resonators inside the capacitor gap of the microwave resonator. Because of this confinement, resonant light contributes much stronger dielectric heating and has a lower probability of generating quasiparticles in the relatively distant inductor where they influence microwave coherence the most. This is aided by the fast quasiparticle recombination rate of Nb. Only at high resonant powers, the quasiparticle effect becomes visible in addition to the local dielectric heating, likely due to generated straylight. We can therefore infer that there are three distinct heating processes in the device (Fig. 4l): i) slow dielectric heating of the substrate from scattered light ii) fast quasiparticle heating in the inductor from straylight iii) fast and local dielectric heating in the transducer capacitance from resonant light.

We summarize these observations by plotting frequency shift (Fig. 4i) and the previously defined effective tempera-

ture T_{eff} (Fig. 4j) at selected times before, during, and after the pulse (marked by arrows in Fig. 4b) as a function of optical peak power. For off-resonant light, we observe blue-shifts up to power levels of $\sim 15 \text{ dBm}$ at all times during the pulse sequence. Increasing power further turns this into a red-shift when the pulse is on, and increases the blue shift when the pulse is off. Resonant light shows a two-fold stronger initial blue shift. After a turning point at about 5 dBm a red-shift starts to dominate. The temperature increase for both resonant and off-resonant light is nonlinear and slows down with increasing pump power. Resonant light causes a ≈ 10 -fold stronger temperature increase.

These data highlight a transition from dielectric dominating at low optical powers to quasi-particle-dominated heating at resonant optical powers above $5\text{-}10 \text{ dBm}$. Such high optical powers already go along with fast in-pulse heating to temperatures well above 1 K (Fig. 4j). These findings are insightful for quantum applications, as it implies that in the quantum-enabled regime ($k_{\text{B}}T_{\text{eff}} \ll \hbar\omega_{\text{b}}$), local dielectric-heating dominates over quasiparticle heating of the superconductor. This result is different to a previous study on a device with a 50 nm NbN film, where off-resonant straylight at the chip interface was concluded to be the dominant heating source [30], suggesting that the device studied here is more resilient against straylight, likely due to the use of a thicker superconducting film. Note, that due to the fast sub μs response of the local dielectric heating, it cannot be mitigated by reducing the duty cycle of the pump. This emphasizes the importance of reducing optical propagation losses as much as possible.

The different relative weights of dielectric and quasiparticle effects for in-cavity light and straylight are illustrated by plotting Δ_{b} vs. T_{eff} (Fig. 4k). Different traces correspond to above selected times during the sequence. For straylight the traces for pulse-off show large frequency blue-shift at low temperature increase. The straylight data traces for pulse-on tend to move towards the curve described by the thermal data. For resonant in-cavity light, however, the trace is shifted to both larger blue-shift and higher effective temperature. This can be interpreted in the sense that straylight causes global heating of the chip that corresponds most closely to an equilibrated thermal state. In-cavity light, however, deviates strongly from the thermal equilibrium because it generates a localized heat source with a stronger dielectric component. An additional reason for the large temperature offset between dielectric and quasiparticles may be the fact that the quasiparticle bath is cooled by the circulator and isolator at the mixing chamber plate (MXC) via the microwave bus line, acting as a heat sink [49].

The heating pathways are summarized in Fig. 4l, showing the quasiparticle (QP) bath, which mostly affects the inductive part of the resonator (L) and the dielectric bath, which primarily affects the capacitor (C). Both baths are driven with different amplitudes by straylight and in-cavity light, and decay to the surrounding chip substrate and package. Finally, the microwave bus couples a cold bath at the cryostat base temperature to the resonator. A detailed analysis of the bath temperatures, coupling rates, and added noise of our trans-

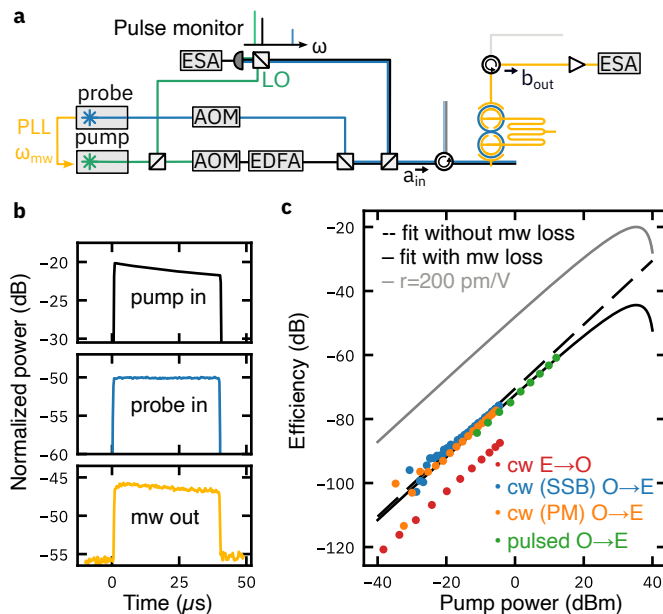


Figure 5. Pulsed transduction and power dependence. (a) For pulsed optical-to-microwave transduction, a blue-detuned probe laser is locked to the pump laser at a frequency offset ω_{mw} . Each laser is pulsed using an acousto-optic modulator (AOM), and the pump laser is additionally amplified with an erbium-doped fiber amplifier (EDFA). Both are combined and sent to the device via a_{in} . The transduced signal is amplified and detected via b_{out} with a spectrum analyzer (ESA). A fraction of the optical input signals is combined with a local oscillator (LO) and detected via a photodiode and an electronic spectrum analyzer (ESA) using heterodyne detection for pulse monitoring. (b) Pulse monitoring time traces for the pump (black), probe (blue) and transduced microwave signal pulse (yellow). (c) Continuous wave microwave-to-optical (red dots) and optical-to-microwave (blue and orange dots) total efficiency versus optical pump power, using heterodyne detection, two offset-locked lasers and a phase modulator, respectively. (green dots) Pulsed optical-to-microwave total efficiency versus optical pump power using two phase-locked lasers. The black line is a model prediction of the efficiency vs. optical pump power taking into account the degradation of the microwave quality factor determined in Figure 29c. (b-d) Time traces of the optical pump and optical input signal beatnotes and detected transduction signal pulse signals for the maximum measured transduction efficiency.

ducer goes beyond the scope of this work and will be subject of future studies.

VI. PULSED OPERATION AND POWER DEPENDENCE

Finally, we investigate the linearity of the transduction efficiency with optical pump power in both pulsed- and continuous wave operation (Fig. 5). For pulsed optical-to-microwave transduction we combine amplified pump pulses with pulses of a weaker probe laser, that is frequency-locked to the blue sideband of the pump laser (Fig. 5a). A fraction of the pump and probe pulses are measured using a calibrated heterodyne detector to determine their respective power levels (Fig. 5b).

In this experiment, the pulse length is decreased from 1 ms to 40 μs with increasing power at decreasing duty cycle to keep the average power constant and maintain good signal-to-noise ratio (SI). The transduced microwave pulses are amplified and recorded on an electronic spectrum analyzer (Fig. 5b). Note that the shapes of the pump and probe pulses are imprinted onto the transduced signal.

Fig. 5c shows conversion efficiency as a function of optical peak pump power for cw microwave-to-optical and optical-to-microwave transduction, as well as pulsed optical-to-microwave transduction. Clearly, all optical-to-microwave data agree within 3 dB and follow a linear trend from pump powers of -30 dBm to +12 dBm. As discussed in Sec. IV, cw microwave-to-optical transduction has a lower total efficiency due to inefficient signal extraction in backward direction.

The pulsed optical-to-microwave transduction data shows clean, linear behavior up to the largest measured power of +12.5 dBm reaching a peak off-chip efficiency of 1×10^{-6} . Higher pump powers could not be delivered to the device, as the fiber-chip efficiency degraded suddenly, likely due to thermal expansion at the fiber coupling point leading to a slight, irreversible misalignment. Another explanation could be the degradation of the optical epoxy at high powers, which was not investigated further. Damage to the transducer device itself can be ruled out since optical and microwave quality factors did not degrade.

To put the efficiencies report here into perspective, we plot a linear trend (Fig. 5c) corresponding to a total-efficiency-per-pump $\eta/P_{pump} = -73$ dB/mW, which is about five orders of magnitude lower than the recently reported value for an optimized LiNbO₃ transducer (-23 dB/mW) [25]. This difference can be largely attributed to the maturity of the LiNbO₃ platform and its highly optimized optical quality factor, which enters the efficiency quadratically. Given the relatively low Pockels coefficient found for our device, an improved BaTiO₃ transducer achieving the previously observed $r = 200$ pm/V [35] would result in more-than 20 dB increase in transduction efficiency (Fig. 5c). We use the measured dependence of microwave quality factor on optical power to estimate when optically-induced microwave decoherence limits transduction efficiency, and find that this happens above 30 dBm, an optical power that is far beyond the range where low-noise transduction is possible.

VII. CONCLUSION

We have presented an integrated, triply resonant electro-optic transducer exploiting the bias-dependent Pockels effect of BaTiO₃. In bidirectional microwave-optical conversion measurements for both continuous-wave and pulsed pumping, we observed high linearity of the transduction efficiency up to pump powers of -2 and +12 dBm, respectively. Under the influence of pulsed optical pumping, heating of the microwave resonator due to quasiparticle and dielectric baths could be distinguished by the induced red and blue microwave frequency shifts, respectively. Overall, optical heating was found to be dominated by in-cavity light, with straylight con-

tributing less than 10% of the temperature increase. Interestingly, we found that for resonant in-cavity light, in contrast to straylight, there is stronger dielectric heating and weaker quasiparticle heating, which we attribute to the different spatial intensity distribution and the use of a thick superconducting film.

Although the demonstrated maximum off-chip pulsed transduction efficiency of -60 dB (-72 dB per mW pump power) is modest, a number of possible improvements in fabrication processes and device design are within reach. If the effective low-temperature Pockels coefficient of only 13 pm/V could be increased by process optimization or strain engineering [44, 50] to the level reported previously in the literature of 200 pm/V [35], efficiency would be enhanced by ~ 20 dB. The optical quality factor is limited by sidewall scattering and absorption and could potentially be improved from the present value of 1×10^5 to the absorption-limited value of 3.8×10^6 [51], providing a further ~ 31 dB increase in efficiency. In addition, adjusting the device geometry should eliminate the mismatch between photonic-molecule resonant splitting 2μ and the microwave resonance frequency ω_b , providing another 4 dB improvement). Using a racetrack geometry instead of circular rings for the optical resonator, large segments of the waveguides would be aligned to the crystal orientation that gives the largest Pockels coefficient, potentially providing 6 dB more efficiency [39]. Finally, off-chip efficiency can be improved by reducing fiber-to-chip coupling losses from -5 to -1 dB through optimized waveguide tapers and chip facets. Achieving all improvements simultaneously would boost microwave-optical cooperativity by up to 56 dB and external efficiency by 4 dB, yielding in principle overall off-chip efficiency approaching unity. Importantly, the implemented device design enables devices with larger vacuum coupling rates g_0 than achievable with LiNbO_3 despite using a material with a significantly larger permittivity. As such, more efficient devices can be realized at a given optical quality factor.

Besides improving efficiency, it is crucial for high-fidelity quantum transduction that input-referenced added noise be maintained below one photon [15, 21, 26, 52]. Our analysis of optically induced broadening of the microwave resonance has shown that the effective temperature of the microwave resonator rapidly increases to over 1 K at 0 dBm peak optical power, corresponding to $n_{\text{add}} \approx 3$. To validate this estimate, we plan to carry out a more detailed investigation of added noise in our transducer [26, 53].

By providing an integrated means to pole the electro-optic material with a dc-bias field, our approach to cavity electro-optics enables the use of materials with nonlinear Pockels behavior. We emphasize that our device design, although implemented in BaTiO_3 , can be transferred with minor modifications to other material platforms, *i.e.*, LiNbO_3 or SrTiO_3 , as the waveguide fabrication relies on dry etching alone. To fully exploit the potential of these complex materials for electro-optic quantum transduction, future studies should investigate methods to both reduce optical loss and maximize the Pockels response at low temperature [50]. Considering the much larger Pockels coefficients of perovskite titanates in compar-

ison to that of LiNbO_3 , this first demonstration opens up a route to microwave-optical quantum transducers with superior performance.

Author Contributions

C.M. designed the transducer with support from A.R.. C.M. and U.D. developed the fabrication process with support from A.R. and A.O.. D.C. and C.M. fabricated the samples with support from U.D., A.O. and A.R.. M.G. and C.M. set up and carried out coupling rate calculations with guidance from T.K.. C.M. performed the measurements with guidance from T.K. and D.I.. C.M. analyzed the data supervised by T.K. and D.I.. T.K. developed the theoretical model of the transducer. T.K. and D.I. designed and built the experimental setup with support from C.M., A.R. and M.G.. C.M. and T.K. wrote the paper with input from all authors. P.S. conceived and supervised the project.

Funding

This work was supported by the European Union Horizon 2020 Programme for Research and Innovation under grant agreement No. 847471 (Marie Curie Co-fund QUSTEC) and SNF QuantEOM (grant No. CRSII5_186364)

Acknowledgments

All samples were fabricated at the Binnig and Rohrer Nanotechnology Center (BRNC) at IBM Research Europe, Zurich. We acknowledge Anel Zulji and Stepha Gamper for manufacturing the sample package and other cryostat components, Michael Stiefel for scanning electron micrographs, Ralph Heller and Andreas Fuhrer for printed circuit design, Hansueli Steinauer for wire bonding, Clarissa Convertino for helpful discussions and substrate preparation, and Stephan Paredes for assistance with cryostat wiring.

Disclosures

The authors declare no conflicts of interest.

Data Availability

Data supporting the plots within this paper and other findings of this study are available through Zenodo at (to be provided). Further information is available from the corresponding author upon reasonable request.

Appendix A: Electro-optic coupling (g_0)

Here, we derive expressions for the electro-optic coupling in our device and provide details on the numerical simulations.

1. Field quantization

First, we recall that the classical electromagnetic energy density ρ_{em} is defined as the absolute value of the Poynting vector [54],

$$\rho_{\text{em}} = \frac{1}{2} (\mathbf{E} \cdot \mathbf{D} + \mathbf{H} \cdot \mathbf{B}), \quad (\text{A1})$$

with electric field \mathbf{E} , electric displacement field $\mathbf{D} = \epsilon_0 \epsilon_r \mathbf{E}$, vacuum permittivity ϵ_0 , and relative permittivity ϵ_r ; and magnetic field \mathbf{H} , magnetic flux density $\mathbf{B} = \mu_0 \mu_r \mathbf{H}$, vacuum permeability μ_0 , and relative permeability μ_r . The vacuum speed of light is $c_0 = 1/\sqrt{\epsilon_0 \mu_0}$. Assuming, for simplicity, an isotropic, non-magnetic ($\mu_r = 1$) dielectric medium with scalar ϵ_r , we can simplify the energy density to

$$\rho_{\text{em}} = \frac{1}{2} \epsilon_0 (\epsilon_r |\mathbf{E}|^2 + c_0^2 |\mathbf{B}|^2). \quad (\text{A2})$$

which is the sum $\rho_{\text{em}} = \rho_e + \rho_m$ of the electrical and magnetic field contributions, i.e.

$$\rho_e = \frac{1}{2} \epsilon_0 \epsilon_r |\mathbf{E}|^2 \quad (\text{A3})$$

$$\rho_m = \frac{1}{2} c_0^2 |\mathbf{B}|^2. \quad (\text{A4})$$

The total electromagnetic energy can then be obtained by integration, i.e.

$$W_{\text{em}} = \int \rho_{\text{em}} dx dy dz \quad (\text{A5})$$

$$W_e = \int \rho_e dx dy dz \quad (\text{A6})$$

$$W_m = \int \rho_m dx dy dz. \quad (\text{A7})$$

For lumped element capacitors and inductors, we have

$$W_e = \frac{1}{2} CV^2 \quad (\text{A8})$$

$$W_m = \frac{1}{2} LI^2, \quad (\text{A9})$$

where C is the capacitance, V is the voltage across the capacitor, L is the inductance, and I is the current flowing through the inductor. In the following, we consider time-averaged energy only, for which holds $\langle W_{\text{em}} \rangle = 2 \langle W_e \rangle$, such that we can focus on the electric energy.

To quantize the cavity electro-optic system, we consider the microwave and optical eigenmodes as harmonic oscillators with ladder operators a and b , and resonance frequencies

ω_a and ω_b , respectively. Their respective uncoupled Hamiltonians are

$$H_a = \hbar \omega_a \left(a^\dagger a + \frac{1}{2} \right), \quad (\text{A10})$$

$$H_b = \hbar \omega_b \left(b^\dagger b + \frac{1}{2} \right). \quad (\text{A11})$$

The quantized electric field operators, in a rotating frame at the optical frequency ω_a , can be defined as [55]

$$\mathbf{E}_a = \sqrt{\frac{\hbar \omega_a}{2 \epsilon_0 U_a}} (a \mathbf{u}_a e^{-i \omega_a t} + a^\dagger \mathbf{u}_a^* e^{+i \omega_a t}), \quad (\text{A12})$$

$$\mathbf{E}_b = \sqrt{\frac{\hbar \omega_b}{2 \epsilon_0 U_b}} (b \mathbf{u}_b + b^\dagger \mathbf{u}_b^*), \quad (\text{A13})$$

with the spatial mode functions \mathbf{u}_i and the effective volumes $U_i = \int \epsilon_r |\mathbf{u}_i|^2 dx dy dz$ for $i \in [a, b]$. Here, it is useful to define the field normalization factors

$$N_i = \sqrt{\frac{\hbar \omega_i}{2 \epsilon_0 U_i}}. \quad (\text{A14})$$

Inserting the expressions (A12) and (A13) for the field operators into the time-averaged energy $W_{\text{em}} = 2W_e$ yields the Hamiltonians (A10) and (A11), respectively.

2. Electro-optic interaction Hamiltonian

Based on refs. [22–24], we first consider the optical electric energy density and express it in terms of the displacement field $D^i = \epsilon_r^{ij} E^j$,

$$\rho_{\text{el,opt}} = \frac{1}{2} \epsilon_0 E_{\text{opt}}^i \epsilon_{r,\text{opt}}^{ij} E_{\text{opt}}^j \quad (\text{A15})$$

$$= \frac{1}{2} \epsilon_0 D_{\text{opt}}^i (\epsilon_{r,\text{opt}}^{-1})^{ij} D_{\text{opt}}^j. \quad (\text{A16})$$

Here and in what follows, it is implicit that indices appearing twice are summed over.

We can now introduce the electro-optic interaction as a perturbation of the optical energy density from a microwave field \mathbf{E}_{mw} that couples to the optical impermeability tensor $(\epsilon_{r,\text{opt}}^{-1})^{ij} \rightarrow (\epsilon_{r,\text{opt}}^{-1})^{ij} + r^{ijk} E_{\text{mw}}^k$. While the first term is just the linear energy density, the second one describes the interaction energy. We can thus define the electro-optic interaction Hamiltonian

$$H_{\text{eo}} = \frac{1}{2} \epsilon_0 \int r^{ijk} D_{\text{opt}}^i D_{\text{opt}}^j E_{\text{mw}}^k dx dy dz. \quad (\text{A17})$$

Moving back to electric fields we have

$$H_{\text{eo}} = \frac{1}{2} \epsilon_0 n_{\text{opt}}^4 \int_{\text{eo}} r^{ijk} E_{\text{opt}}^i E_{\text{opt}}^j E_{\text{mw}}^k dx dy dz, \quad (\text{A18})$$

where \int_{eo} denotes the integral over the volume of the electro-optic material, where $r \neq 0$. Inserting the field operators \mathbf{E}_a

and \mathbf{E}_b from (A12) and (A13) for the optical and microwave modes, respectively, we obtain

$$H_{eo} = \frac{1}{2} \epsilon_0 n_{\text{opt}}^4 \int_{\text{eo}} r^{ijk} E_a^i E_a^j E_b^k dx dy dz \quad (\text{A19})$$

$$= \epsilon_0 n_{\text{opt}}^4 N_a^2 N_b \cdot \int_{\text{eo}} r^{ijk} (u_a^i)^* u_a^j a^\dagger a (u_b^k b + (u_b^k)^* b^\dagger) dx dy dz \quad (\text{A20})$$

In the last equation, we only kept terms conserving the optical photon number. We finally arrive at an expression for the vacuum coupling strength g_0 . Since the microwave spatial mode function u_b is real-valued, we have $H_{eo} = \hbar g_0 a^\dagger a (b + b^\dagger)$ single optical ring resonator, with [23]

$$\hbar g_0 = \epsilon_0 n_{\text{opt}}^4 N_a^2 N_b \int_{\text{eo}} r^{ijk} (u_a^i)^* u_a^j u_b^k dx dy dz. \quad (\text{A21})$$

Considering only a single in-plane field component, as is approximately the case in our device, we get

$$\hbar g_0 = \epsilon_0 r n_{\text{opt}}^4 N_a^2 N_b \int_{\text{eo}} |u_a|^2 u_b dx dy dz. \quad (\text{A22})$$

We note that this describes the coupling between the microwave mode and one of the optical ring resonators. The full electro-optic interaction Hamiltonian contains the contributions of both ring resonators, and takes into account that the $\lambda/2$ -type microwave mode function u_b (Fig. 7a) is equal and opposite at both rings, i.e.

$$H_{eo} = \hbar g_0 (a_1^\dagger a_1 - a_2^\dagger a_2) (b + b^\dagger). \quad (\text{A23})$$

3. Separating longitudinal and cross-sectional integration

Since the overlap only happens in the active material of the optical rings, we can separate the integration into a longitudinal (dz) and cross sectional part ($dx dy$). For the longitudinal integral along one optical ring resonator with radius R , we get (neglecting curvature)

$$\int r dz = r \alpha_{\text{overlap}} L_{\text{opt}} \quad (\text{A24})$$

with total optical length of $L_{\text{opt}} = 2\pi R$ being the ring circumference. The factor α_{overlap} describes the effective overlap fraction of the microwave and optical fields, which takes into account the angle dependence of the Pockels effect. Motivated by the results reported in [35] and [39], we model the angular dependence as a sinusoidal function with a maximum every 90° (blue solid line in Fig. 6). The blue areas under the curves mark the angular interval of the rings which is covered by the transducer electrodes (Fig. 6a) and tuning electrodes (Fig. 6b). The transducer electrodes cover an interval of $2\pi \alpha_{\text{coverage}} = 2\pi \cdot 0.91$, but due to the angle dependence the effective overlap is only $\alpha_{\text{overlap}} = 0.42$. We thus obtain

$$\hbar g_0 = L_{\text{opt}} \alpha_{\text{overlap}} \epsilon_0 r n_{\text{opt}}^4 N_a^2 N_b \cdot \int_{\text{eo}} |u_a|^2 |u_b| dx dy. \quad (\text{A25})$$

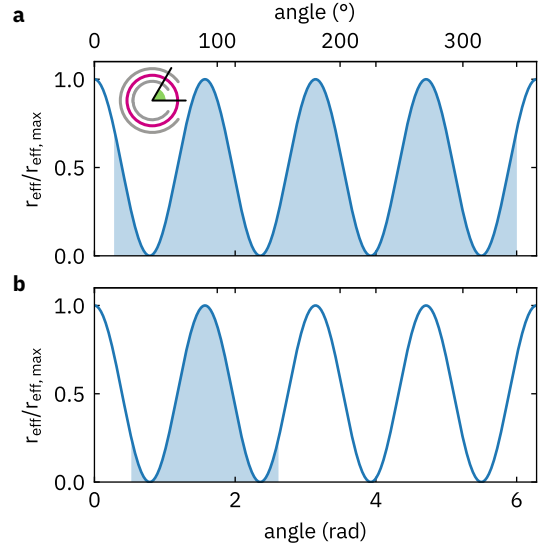


Figure 6. **Model for angular dependence of Pockels effect.** Model for the angular dependence of the Pockels effect (blue solid line) and visualization of the overlap factor α_{overlap} as the blue shaded area under the curve for (a) the transducer electrode and (b) the tuning electrode, with 42.0% and 13.2%, respectively.

Note, that we replaced the complex amplitude of the microwave field by its absolute value to ensure that no arbitrary phase in the numerical simulation leads to issues with the integration. Furthermore the eo subscript for the integral denotes that we only integrate over the electro-optic material cross-sectional surface, as the electro-optic coefficients vanishes everywhere else.

The frequency pulling factor $G = \partial \omega_{\text{opt}} / \partial V = g_0 / V_{\text{zpf}}$ can be calculated analogously. We note that $N_b u_b$ is the zero-point microwave electric field. Noting that

$$\frac{N_b u_b}{V_{\text{zpf}}} = \frac{E_b}{V_{\text{sim}}} \quad (\text{A26})$$

where for E_b we use the simulated microwave field for the applied voltage V_{sim} , we get

$$G = \frac{L_{\text{opt}} \alpha_{\text{overlap}} \epsilon_0 r n_{\text{opt}}^4 N_a^2}{\hbar V_{\text{sim}}} \int_{\text{eo}} |u_a|^2 |E_b| dx dy \quad (\text{A27})$$

The only quantities left to compute are the field normalization factors. For the optics this is straightforward by integrating the cross-sectional field distribution,

$$N_a = \sqrt{\frac{\hbar \omega_a}{[2 \epsilon_0 L_{\text{opt}} \int n_{\text{opt}}^2 |\mathbf{u}_a|^2 dx dy]}}. \quad (\text{A28})$$

4. Microwave equivalent circuit

An analogous normalization factor equation as (A28) holds for the microwave field in principle as well, but would require

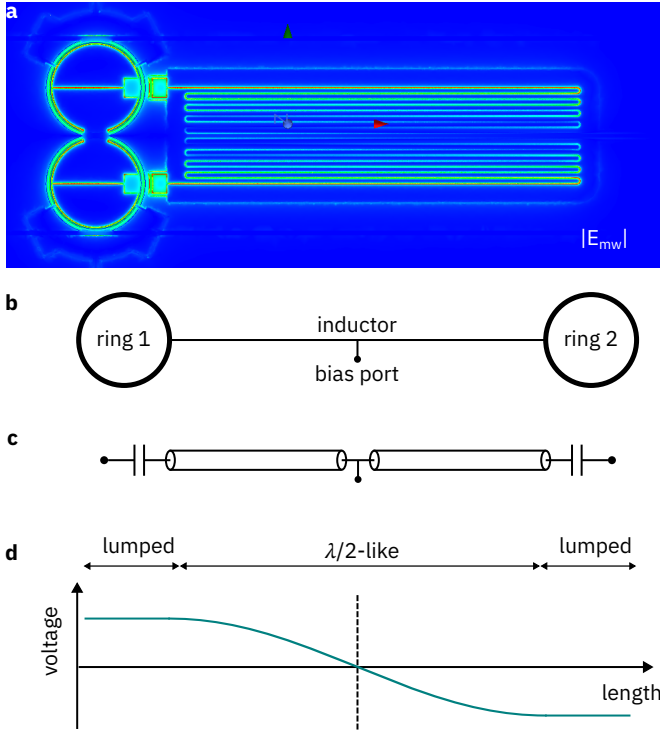


Figure 7. **Microwave mode.** (a) 3d-finite element Ansys HFSS eigenmode simulation of the microwave mode field distribution. (b) Schematic of the electrical circuit with unfolded meander inductor. (c) Transmission line representation of the circuit with lumped (ring) capacitances at each end and a $\lambda/2$ -type field distribution in the transmission line that vanishes at the bias port, as shown in (d).

simulating the whole microwave mode. Instead, we only simulate the fraction of the microwave mode in the transducer electrode, and therefore have to normalize to only the energy fraction that is contained in that transducer electrode. We do this by introducing the participation ratio

$$\rho_c = \frac{C_{\text{ring}}}{C_{\text{ring}} + C_{L,\text{mw}}}, \quad (\text{A29})$$

which describes the fraction of the total electric field energy of the microwave resonator that is contained in the transducer electrodes, i.e. the rings. As illustrated in the transducer equivalent circuit (Fig. 8, C_{ring} is the electrode capacitance at each ring and $C_{L,\text{mw}}$ is the parasitic capacitance of each electrode. Additionally, we need to take into account that the transducer electrode only overlaps with the fraction α_{coverage} of the optical ring resonator, giving the corrected normalization

$$N_b = \sqrt{\frac{\rho_c \hbar \omega_b}{2\epsilon_0 L_{\text{opt}} \alpha_{\text{coverage}} \int \epsilon_r |\mathbf{u}_b|^2 dx dy}}. \quad (\text{A30})$$

To obtain the participation ratio ρ_c , we first determine the capacitance of each ring electrode C_{ring} . On the one hand, we can do this in an electrostatic simulation of the whole device using the finite-element solver Ansys Maxwell. The resulting dc-capacitances of the different circuit elements are

| fF | $C_{\text{ring},2}$ | C_{ind} | $C_{\text{ring},1}$ | C_{ground} | $C_{\text{tune},1}$ | $C_{\text{tune},2}$ |
|---------------------|---------------------|------------------|---------------------|---------------------|---------------------|---------------------|
| $C_{\text{ring},2}$ | 57.3 | -2.1 | -1.6 | -36.8 | -0.4 | -16.4 |
| C_{ind} | -2.1 | 177.4 | -2.1 | -170.5 | -1.4 | -1.4 |
| $C_{\text{ring},1}$ | -1.6 | -2.1 | 57.3 | -36.8 | -16.5 | -0.4 |
| C_{ground} | -36.8 | -170.5 | -36.8 | 343.2 | -49.5 | -49.5 |
| $C_{\text{tune},1}$ | -0.4 | -1.4 | -16.5 | -49.5 | 67.8 | -0.1 |
| $C_{\text{tune},2}$ | -16.4 | -1.4 | -0.4 | -49.5 | -0.1 | 67.7 |

Table I. **Simulated dc capacitances.** 3d-finite element simulation of dc-capacitances for the electro-optic transducer using Ansys Maxwell. The active material permittivity is set to $\epsilon_r = 200$ in this case.

| C (fF) | L (nH) |
|----------|----------|
| 69.0 | 7.4 |

Table II. **Simulated microwave equivalent circuit parameters.** Fit results of the fit of equation A34 to the data obtained from 3d-finite element eigenmode simulations of the the electro-optic transducer with a parallel capacitance with Ansys Maxwell (Fig. 9a).

listed in Table I. The ring capacitance is about 57.3 fF. On the other hand, we can directly compute the capacitance from the field distribution \mathbf{u}_b of a Comsol finite-element simulation by equating the capacitive energy with the applied simulation voltage to the energy of the simulated field,

$$W_{b,e} = \frac{1}{2} C_{\text{ring}} V_{\text{sim}}^2 \quad (\text{A31})$$

$$= \frac{1}{2} \epsilon_0 \alpha_{\text{coverage}} 2\pi R \int \epsilon_r |\mathbf{u}_b|^2 dx dy. \quad (\text{A32})$$

It is important to note here, that we now have a factor of $1/2$ for the electrical energy term, as we are really only looking at the capacitive part of the energy. This can be solved for the ring capacitance,

$$C_{\text{ring}} = \frac{\epsilon_0 \alpha_{\text{coverage}} 2\pi R}{V_{\text{sim}}^2} \int \epsilon_r |\mathbf{u}_b|^2 dx dy. \quad (\text{A33})$$

Using a Comsol cross-sectional simulation, we obtain 61.1 fF for the ring electrode, which is fairly close to the value obtained from the three-dimensional dc finite element simulation (Table I).

We are now only missing the value for either the equivalent circuit capacitance C or the microwave stray capacitance of the inductor arm $C_{L,\text{mw}}$. The latter can in principle be estimated from the dc-capacitances listed in Table I.



Figure 8. **Participation ratio.** (a) Standard equivalent circuit and (b) extended circuit representation of the transducer device. The ring capacitances C_{ring} go from one inductor end to ground, and the stray capacitance from the inductor is modeled as parallel capacitances $C_{L,\text{mw}}$, also to ground.

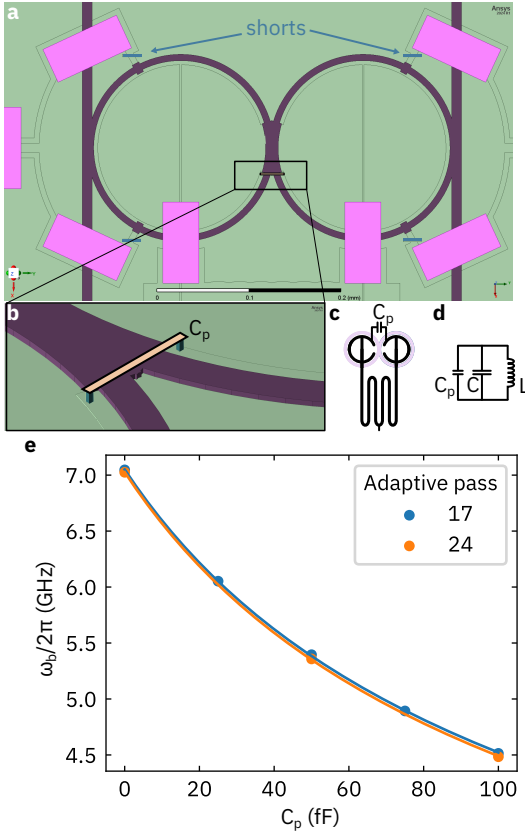


Figure 9. **Geometric inductance and capacitance extraction using a parallel capacitance.** (a) Ansys HFSS simulation setup view of the capacitive part of the circuit with patches (blue) to short the coupling electrodes to ground. (b) Out-of-plane pins (blue) connected with a 2D-sheet (orange) which is defined as a lumped element boundary condition with capacitance C_p . (c) Schematic representation of the modified device circuit with the added parallel capacitance C_p between the ring electrodes. (d) Equivalent circuit representation with the parallel capacitance in addition to the equivalent capacitance C and inductance of the device L . (e) Resonance frequency of the device as a function of parallel capacitance C_p using the mesh after 17 (blue dots) and 24 adaptive passes (orange dots) and fit to equation A34.

An accurate value for the inductance L and the equivalent circuit capacitance C can be obtained by performing a 3d finite element eigenmode simulation of the full circuit, but with an added parallel capacitance C_p . The simulation setup is shown in Fig. 9a, where the coupling capacitances were set to ground by shorting with small patches (blue). The parallel capacitance is then implemented as a bridge between the two ring electrodes at the shortest possible distance (Fig. 9b). The bridge is implemented using two blocks (blue) that connect the ring electrodes to a two-dimensional sheet, on which a lumped element capacitance boundary condition with value C_p is defined. A schematic of the modified device circuit is shown in Fig. 9c. Effectively, this represents an additional parallel capacitance C_p to the equivalent circuit capacitance C defined in Fig. 8, as drawn in Fig. 9d. The resonance frequency of this modified circuit is then simulated as a function

of the parallel capacitance C_p , as shown in Fig. 9e. The advantage of using a lumped element is, that the mesh for the simulation only needs to be calculated once, and can then be used to simulate for all values of C_p . The observed dependence of the resonance frequency on the the parallel capacitance is modeled as

$$\omega_b = \sqrt{\frac{1}{L(C + C_p)}}, \quad (\text{A34})$$

with the inductance L and the equivalent capacitance C of the device as fit parameters. The results are listed in Table II. We can then use the fact that the circuit is symmetric, and together with the rules for series and parallel capacitances we have

$$C = \frac{C_{\text{ring}} + C_{L,\text{mw}}}{2}, \quad (\text{A35})$$

which we can solve for the inductor's capacitance

$$C_{L,\text{mw}} = 2C - C_{\text{ring}}, \quad (\text{A36})$$

which equates to $C_{L,\text{mw}} = 80.7 \text{ fF}$ using the value of C_{ring} from Table I. With this, we arrive at a participation ratio of $\rho_c = 0.43$.

For the zero-point fluctuations across the ring electrodes, the relevant capacitance is $C_{\text{ring}} + C_{L,\text{mw}} = 2C$. The effective microwave voltage operator [56] can thus be written as

$$V_b = V_{\text{zpf}} (b + b^\dagger), \quad (\text{A37})$$

with zero-point voltage

$$V_{\text{zpf}} = \sqrt{\frac{\hbar\omega_b}{4C}}. \quad (\text{A38})$$

We note that for the calculation of g_0 , Eq. (A22) was used.

5. Incorporating scaling with material permittivity

In order to fairly compare the vacuum coupling strength of the same device design and cross-sectional geometry but for different active materials with similar optical properties but sometimes vastly different permittivities ($\epsilon_{r,\text{LiNbO}_3} = 30$, $\epsilon_{r,\text{BaTiO}_3} = 200$, $\epsilon_{r,\text{SrTiO}_3} \approx 20000$), we incorporate the scaling of the inductor, which affects both the inductance and stray capacitance of the circuit, and thereby also the total capacitance and participation ratio. We do this, by requiring a constant resonance frequency ω_b of the transducer

$$\omega_b = \frac{1}{\sqrt{LC}}. \quad (\text{A39})$$

We then assume that by varying the length of the meander inductor wire by the factor α_{ind} , its inductance and capacitance vary proportionally, such that the resonance frequency scales as

$$\omega_b = \frac{1}{\sqrt{\alpha_{\text{ind}}L(C_{\text{ring}} + \alpha_{\text{ind}}C_{L,\text{mw}})/2}}. \quad (\text{A40})$$

We can solve this quadratic equation for α_{ind} of the form $0 = ax^2 + bx + c$ with the coefficients

$$a = LC_{L,\text{mw}} \quad (\text{A41})$$

$$b = LC_{\text{ring}} \quad (\text{A42})$$

$$c = -\frac{2}{\omega_b^2}. \quad (\text{A43})$$

The inductor scaling parameter is then determined via

$$\alpha_{\text{ind}} = \frac{-b \pm \sqrt{b^2 - 4ac}}{2a}, \quad (\text{A44})$$

where we use the positive solution.

Appendix B: Linear system response

1. Open coupled mode system

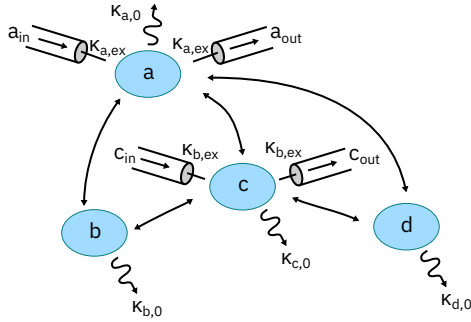


Figure 10. **Open coupled mode system.** Resonant modes $i \in \{a, b, c, d, \dots\}$ are modeled as quantum harmonic oscillators with intrinsic loss rates $\kappa_{i,0}$ and external coupling rates $\kappa_{i,\text{ex}}$ to the input and output modes $i_{\text{in/out}}$. Additionally, they are coupled to each other in a pairwise manner as indicated by the black arrows.

In this section we give an introduction to the input-output formalism and coupled mode theory required to describe the linear response of the cavity electro-optic system studied in this work.

As illustrated in Fig. 10, we describe the system as a collection of resonant modes $i \in \{a, b, c, d, \dots\}$ with resonance frequencies ω_i and internal loss rates $\kappa_{i,0}$. Each mode is coupled to its corresponding in- and output bus mode $i_{\text{in/out}}$ at the external coupling rate $\kappa_{i,\text{ex}}$. Additionally, there can be pairwise coherent couplings between any of the modes and with a certain phase, as indicated by the black arrows.

In a first step, the hamiltonian dynamics of the system are defined, which consist of the eigenvalues of each mode $\hbar\omega_i i^\dagger i$ and the pairwise couplings $\hbar\nu_{ij} (i^\dagger j + j^\dagger i)$:

$$H_i = \sum_i \hbar\omega_i i^\dagger i + \sum_{ij} \hbar\nu_{ij} i^\dagger j. \quad (\text{B1})$$

The open system dynamics from coupling to bus modes or e.g. thermal baths are introduced by including the often called

noise operator \mathcal{L} in the Quantum Langevin equations of motion for an operator X [57, 58]:

$$\dot{X} = \frac{1}{i\hbar} [X, H] + \mathcal{L}X. \quad (\text{B2})$$

We can regroup these equations of motion in a dynamical and input-output part by defining the state vector $\mathbf{q} = (a, a^\dagger, b, b^\dagger, \dots)$, input mode vector $\mathbf{q}_{\text{in}} = (a_{\text{in}}, a_{\text{in}}^\dagger, b_{\text{in}}, b_{\text{in}}^\dagger, \dots)$, output mode vector $\mathbf{q}_{\text{out}} = (a_{\text{out}}, a_{\text{out}}^\dagger, b_{\text{out}}, b_{\text{out}}^\dagger, \dots)$, the dynamical matrix M' and input-output matrix K :

$$\dot{\mathbf{q}} = M'\mathbf{q} + K\mathbf{q}_{\text{in}}. \quad (\text{B3})$$

Each line of this matrix equation is defined by the quantum Langevin equation of motion for each state vector component:

$$\dot{q}_i = \frac{1}{i\hbar} [q_i, H] + \mathcal{L}q_i \quad (\text{B4})$$

or

$$\dot{q}_i = \frac{i}{\hbar} [H, q_i] + \mathcal{L}q_i, \quad (\text{B5})$$

where $+\mathcal{L}q_i$ are the entries of the input output matrix K . We can further use the identify:

$$\dot{q}_i^\dagger = (\dot{q}_i)^\dagger. \quad (\text{B6})$$

By performing a fourier transformation at frequency ω ($-\omega$ for conjugated operators), we obtain the frequency domain equations of motion with the redefined dynamical matrix $M = (-i\omega\mathbb{I} - M')$:

$$M\mathbf{q} = K\mathbf{q}_{\text{in}}. \quad (\text{B7})$$

Note, that here and below, the vector denote frequency-domain operators at frequency ω ($-\omega$ for conjugated operators):

$$\mathbf{q} = (a(\omega), a^\dagger(-\omega), b(\omega), b^\dagger(-\omega), \dots). \quad (\text{B8})$$

Eq. B7 can be inverted to solve for the state vector \mathbf{q} :

$$\mathbf{q} = M^{-1}K\mathbf{q}_{\text{in}}. \quad (\text{B9})$$

To obtain the linear response of the system, we need to relate the output fields to the input fields and system modes using the input-output relation:

$$\mathbf{q}_{\text{out}} = \mathbf{q}_{\text{in}} - K^T\mathbf{q}. \quad (\text{B10})$$

Putting everything together, we obtain the output as a linear function of the input:

$$\mathbf{q}_{\text{out}} = \mathbf{q}_{\text{in}} - K^T M^{-1} K \mathbf{q}_{\text{in}}, \quad (\text{B11})$$

allowing us to define the scattering matrix of the system:

$$S = (\mathbb{I} - K^T M^{-1} K). \quad (\text{B12})$$

2. Photonic molecule with forward-backward scattering

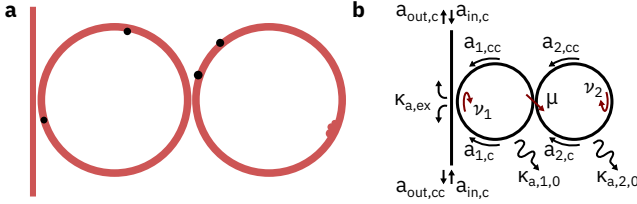


Figure 11. **Photonic molecule with backscattering.** (a) Physical representation of photonic molecule circuit, consisting of two coupled optical rings. Imperfections leading to backscattering such as scattering site on or in the waveguide (black dots) or waveguide cross-section irregularities (bottom right) are illustrated. (b) Coupling and loss rates between the involved clockwise and counterclockwise propagating resonator modes $a_{i,c}$, $a_{i,cc}$ ($i \in \{1, 2\}$) and in- and output modes a_{in} , a_{out} .

Now, we can apply the input-output and coupled mode formalism derived above to the optical system in the transducer device studied in this work. As shown in Fig. 11a, the physical system consists of two coupled ring resonators, of which one is evanescently coupled to the optical bus waveguide. The optical resonator can have imperfections such as particles or other scattering sites on top or in the waveguide (black dots), or waveguide cross section variations (line edge roughness). These imperfections can lead to a coupling between the ideally degenerate and uncoupled forward- ($a_{i,c}$) and backward propagating optical modes ($a_{i,cc}$) for $i \in \{1, 2\}$ (Fig. 11b).

We start out with the optical system Hamiltonian:

$$\begin{aligned} H_a = & + \hbar\omega_1 a_{1,c}^\dagger a_{1,c} + \hbar\omega_1 a_{1,cc}^\dagger a_{1,cc} \\ & + \hbar\omega_2 a_{2,c}^\dagger a_{2,c} + \hbar\omega_2 a_{2,cc}^\dagger a_{2,cc} \\ & - \hbar\mu \left(a_{1,c} + a_{1,c}^\dagger \right) \left(a_{2,cc} + a_{2,cc}^\dagger \right) \\ & - \hbar\mu \left(a_{1,cc} + a_{1,cc}^\dagger \right) \left(a_{2,c} + a_{2,c}^\dagger \right) \\ & - \hbar\nu_1 \left(a_{1,c} + a_{1,c}^\dagger \right) \left(a_{1,cc} + a_{1,cc}^\dagger \right) \\ & - \hbar\nu_2 \left(a_{2,c} + a_{2,c}^\dagger \right) \left(a_{2,cc} + a_{2,cc}^\dagger \right), \end{aligned} \quad (\text{B13})$$

where μ and ν_i with $i \in \{1, 2\}$ denote the ring-ring and forward-backward coupling rates, respectively.

We first omit the very fast rotating terms, that are rotating at twice the optical frequency, leaving us with:

$$\begin{aligned} H_a = & + \hbar\omega_1 a_{1,c}^\dagger a_{1,c} + \hbar\omega_1 a_{1,cc}^\dagger a_{1,cc} \\ & + \hbar\omega_2 a_{2,c}^\dagger a_{2,c} + \hbar\omega_2 a_{2,cc}^\dagger a_{2,cc} \\ & + \hbar\omega_b b^\dagger b \\ & - \hbar\mu \left(a_{1,c} a_{2,cc}^\dagger + a_{1,c}^\dagger a_{2,cc} \right) \\ & - \hbar\mu \left(a_{1,cc} a_{2,c}^\dagger + a_{1,cc}^\dagger a_{2,c} \right) \\ & - \hbar\nu_1 \left(a_{1,c} a_{1,cc}^\dagger + a_{1,c}^\dagger a_{1,cc} \right) \\ & - \hbar\nu_2 \left(a_{2,c} a_{2,cc}^\dagger + a_{2,c}^\dagger a_{2,cc} \right). \end{aligned} \quad (\text{B14})$$

In a rotating frame at the laser frequency, we have

$$\begin{aligned} H_a = & - \hbar\Delta_{p,1} a_{1,c}^\dagger a_{1,c} - \hbar\Delta_{p,1} a_{1,cc}^\dagger a_{1,cc} \\ & - \hbar\Delta_{p,2} a_{2,c}^\dagger a_{2,c} - \hbar\Delta_{p,2} a_{2,cc}^\dagger a_{2,cc} \\ & + \hbar\omega_b b^\dagger b \\ & - \hbar\mu \left(a_{1,c} a_{2,cc}^\dagger + a_{1,c}^\dagger a_{2,cc} \right) \\ & - \hbar\mu \left(a_{1,cc} a_{2,c}^\dagger + a_{1,cc}^\dagger a_{2,c} \right) \\ & - \hbar\nu_1 \left(a_{1,c} a_{1,cc}^\dagger + a_{1,c}^\dagger a_{1,cc} \right) \\ & - \hbar\nu_2 \left(a_{2,c} a_{2,cc}^\dagger + a_{2,c}^\dagger a_{2,cc} \right), \end{aligned} \quad (\text{B15})$$

with the optical detunings $\Delta_{p,1} = \omega_p - \omega_1$ and $\Delta_{p,2} = \omega_p - \omega_2$.

We define the input, output and cavity state vectors:

$$\mathbf{q}_a = [a_{1,c} \ a_{1,cc} \ a_{2,c} \ a_{2,cc}] \quad (\text{B16})$$

$$\mathbf{q}_{a,\text{in}} = [a_{\text{in},c} \ a_{\text{in},cc} \ 0 \ 0] \quad (\text{B17})$$

$$\mathbf{q}_{a,\text{out}} = [a_{\text{out},c} \ a_{\text{out},cc} \ 0 \ 0]. \quad (\text{B18})$$

Following the conventions outlined in Fig. 11b we define the optical input-output matrix:

$$K_a = \begin{bmatrix} \sqrt{\kappa_{a,\text{ex}}} & 0 & 0 & 0 \\ 0 & \sqrt{\kappa_{a,\text{ex}}} & 0 & 0 \\ 0 & 0 & 0 & 0 \\ 0 & 0 & 0 & 0 \end{bmatrix}, \quad (\text{B19})$$

and the optical time-domain dynamic matrix:

$$\begin{aligned} M'_a = & \begin{bmatrix} +i\Delta_{p,1} & +i\nu_1 & 0 & +i\mu \\ +i\nu_1 & +i\Delta_{p,1} & +i\mu & 0 \\ 0 & +i\mu & +i\Delta_{p,2} & +i\nu_2 \\ +i\mu & 0 & +i\nu_2 & +i\Delta_{p,2} \end{bmatrix} \\ & + \begin{bmatrix} -\frac{\kappa_1}{2} & 0 & 0 & 0 \\ 0 & -\frac{\kappa_1}{2} & 0 & 0 \\ 0 & 0 & -\frac{\kappa_2}{2} & 0 \\ 0 & 0 & 0 & -\frac{\kappa_2}{2} \end{bmatrix}, \end{aligned} \quad (\text{B20})$$

with the total optical linewidths $\kappa_1 = \kappa_{a,1,0} + \kappa_{a,\text{ex}}$ and $\kappa_2 = \kappa_{a,2,0}$. The frequency-domain dynamical matrix can then be written as:

$$M_a(\omega) = \begin{bmatrix} \frac{1}{\chi_1(\omega)} & -i\nu_1 & 0 & -i\mu \\ -i\nu_1 & \frac{1}{\chi_1(\omega)} & -i\mu & 0 \\ 0 & -i\mu & \frac{1}{\chi_2(\omega)} & -i\nu_2 \\ -i\mu & 0 & -i\nu_2 & \frac{1}{\chi_2(\omega)} \end{bmatrix}, \quad (\text{B21})$$

with the response functions:

$$\chi_1(\omega) = \frac{1}{\kappa_1/2 - i(\omega + \Delta_{p,1})} \quad (\text{B22})$$

$$\chi_2(\omega) = \frac{1}{\kappa_2/2 - i(\omega + \Delta_{p,2})}. \quad (\text{B23})$$

For a single-tone optical transmission or reflection measurement, we set $\omega = 0$, and ω_p corresponds to the optical probe frequency. With this, we can calculate the S-matrix elements using Eq. B12.

3. Transduction model

We can use the formalism derived in Sec. B1 and applied to the optical system of the transducer in Sec. B2 to describe the full transduction process by including the microwave resonator and the electro-optic interaction. For clarity, we separate the system in an optic, microwave, and electro-optic part:

$$H = H_a + H_b + H_{\text{eo}}, \quad (\text{B24})$$

with:

$$H_b = \hbar\omega_b b^\dagger b \quad (\text{B25})$$

and the electro-optic interaction hamiltonian in the uncoupled optical basis:

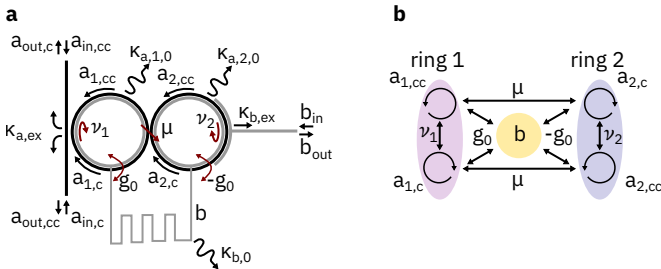


Figure 12. Full transduction model.

$$\begin{aligned} H_{\text{eo}} = & -\frac{1}{2}\hbar g_0 (a_{1,c} + a_{1,c}^\dagger) (a_{1,c} + a_{1,c}^\dagger) (b + b^\dagger) \\ & -\frac{1}{2}\hbar g_0 (a_{1,cc} + a_{1,cc}^\dagger) (a_{1,cc} + a_{1,cc}^\dagger) (b + b^\dagger) \\ & +\frac{1}{2}\hbar g_0 (a_{2,c} + a_{2,c}^\dagger) (a_{2,c} + a_{2,c}^\dagger) (b + b^\dagger) \\ & +\frac{1}{2}\hbar g_0 (a_{2,cc} + a_{2,cc}^\dagger) (a_{2,cc} + a_{2,cc}^\dagger) (b + b^\dagger). \end{aligned} \quad (\text{B26})$$

Note, that in this basis the phase matching condition is naturally incorporated in the coupling via the antisymmetric sign between the two rings. With the same argument as in Sec. B2, we omit terms rotating at twice the optical frequency:

$$\begin{aligned} H_{\text{eo}} = & -\frac{1}{2}\hbar g_0 (a_{1,c}a_{1,c}^\dagger + a_{1,c}^\dagger a_{1,c}) (b + b^\dagger) \\ & -\frac{1}{2}\hbar g_0 (a_{1,cc}a_{1,cc}^\dagger + a_{1,cc}^\dagger a_{1,cc}) (b + b^\dagger) \\ & +\frac{1}{2}\hbar g_0 (a_{2,c}a_{2,c}^\dagger + a_{2,c}^\dagger a_{2,c}) (b + b^\dagger) \\ & +\frac{1}{2}\hbar g_0 (a_{2,cc}a_{2,cc}^\dagger + a_{2,cc}^\dagger a_{2,cc}) (b + b^\dagger). \end{aligned} \quad (\text{B27})$$

Next, we linearize the electro-optic interaction by assuming that the optical fields have a large classical amplitude plus a small quantum fluctuation $a \rightarrow \alpha + a$ with $\alpha = \langle a \rangle$:

$$a \rightarrow \alpha + a, \quad (\text{B28})$$

transforming the quadratic optical part to the sum:

$$\begin{aligned} aa^\dagger & \rightarrow (\alpha + a) (\bar{\alpha} + a^\dagger) = |\alpha|^2 + \alpha a^\dagger + \bar{\alpha} a + aa^\dagger \\ a^\dagger a & \rightarrow (\bar{\alpha} + a^\dagger) (\alpha + a) = |\alpha|^2 + \alpha a^\dagger + \bar{\alpha} a + a^\dagger a \end{aligned} \quad (\text{B29})$$

We omit the quadratic terms aa^\dagger and $a^\dagger a$, as well as the electro-optic spring effect term $|\alpha|^2$. The latter may be incorporated in the model by including it in the optical detuning, if necessary. This leaves us with the linearised laser-rotating-frame hamiltonian:

$$H_{\text{eo}} = -\hbar g_0 (\alpha_{1,c} a_{1,c}^\dagger + \bar{\alpha}_{1,c} a_{1,c}) (b + b^\dagger) \quad (\text{B30})$$

$$-\hbar g_0 (\alpha_{1,cc} a_{1,cc}^\dagger + \bar{\alpha}_{1,cc} a_{1,cc}) (b + b^\dagger) \quad (\text{B31})$$

$$+\hbar g_0 (\alpha_{2,c} a_{2,c}^\dagger + \bar{\alpha}_{2,c} a_{2,c}) (b + b^\dagger) \quad (\text{B32})$$

$$+\hbar g_0 (\alpha_{2,cc} a_{2,cc}^\dagger + \bar{\alpha}_{2,cc} a_{2,cc}) (b + b^\dagger). \quad (\text{B33})$$

With the full system Hamiltonian derived, we can now apply the formalism to obtain the scattering matrix. However, because we will now consider the response at a general

Fourier frequency ω and not just at $\omega = 0$ as in Sec. B 2, we have to consider the dynamics of the adjunct operators i^\dagger as well, whose equations of motion can be derived analogously using Eq. B 6. We thus define the state operators:

$$\mathbf{q} = \begin{bmatrix} a_{1,c} & a_{1,c}^\dagger & a_{1,cc} & a_{1,cc}^\dagger & a_{2,c} & a_{2,c}^\dagger & a_{2,cc} & a_{2,cc}^\dagger & b & b^\dagger \end{bmatrix} \quad (\text{B34})$$

$$\mathbf{q}_{\text{in}} = \begin{bmatrix} a_{\text{in},c} & a_{\text{in},c}^\dagger & a_{\text{in},cc} & a_{\text{in},cc}^\dagger & 0 & 0 & 0 & 0 & b_{\text{in}} & b_{\text{in}}^\dagger \end{bmatrix} \quad (\text{B35})$$

$$\mathbf{q}_{\text{out}} = \begin{bmatrix} a_{\text{out},c} & a_{\text{out},c}^\dagger & a_{\text{out},cc} & a_{\text{out},cc}^\dagger & 0 & 0 & 0 & 0 & b_{\text{out}} & b_{\text{out}}^\dagger \end{bmatrix}. \quad (\text{B36})$$

The input-output matrix for the full system is given by:

$$K = \begin{bmatrix} \sqrt{\kappa_{a,\text{ex}}} & 0 & 0 & 0 & 0 & 0 & 0 & 0 & 0 & 0 \\ 0 & \sqrt{\kappa_{a,\text{ex}}} & 0 & 0 & 0 & 0 & 0 & 0 & 0 & 0 \\ 0 & 0 & \sqrt{\kappa_{a,\text{ex}}} & 0 & 0 & 0 & 0 & 0 & 0 & 0 \\ 0 & 0 & 0 & \sqrt{\kappa_{a,\text{ex}}} & 0 & 0 & 0 & 0 & 0 & 0 \\ 0 & 0 & 0 & 0 & \sqrt{\kappa_{a,\text{ex}}} & 0 & 0 & 0 & 0 & 0 \\ 0 & 0 & 0 & 0 & 0 & \sqrt{\kappa_{a,\text{ex}}} & 0 & 0 & 0 & 0 \\ 0 & 0 & 0 & 0 & 0 & 0 & \sqrt{\kappa_{b,\text{ex}}} & 0 & 0 & 0 \\ 0 & 0 & 0 & 0 & 0 & 0 & 0 & \sqrt{\kappa_{b,\text{ex}}} & 0 & 0 \\ 0 & 0 & 0 & 0 & 0 & 0 & 0 & 0 & \sqrt{\kappa_{b,\text{ex}}} & 0 \end{bmatrix}. \quad (\text{B37})$$

The time-domain dynamical matrix is:

$$M' = M'_a + M'_b + M'_{\text{eo}}, \quad (\text{B38})$$

with the optical time-domain matrix:

$$M'_a = \begin{bmatrix} +i\Delta_{p,1} & 0 & +i\nu_1 & 0 & 0 & 0 & +i\mu & 0 & 0 & 0 \\ 0 & -i\Delta_{p,1} & 0 & -i\bar{\nu}_1 & 0 & 0 & 0 & -i\mu & 0 & 0 \\ +i\nu_1 & 0 & +i\Delta_{p,1} & 0 & +i\mu & 0 & 0 & 0 & 0 & 0 \\ 0 & -i\bar{\nu}_1 & 0 & -i\Delta_{p,1} & 0 & -i\mu & 0 & 0 & 0 & 0 \\ 0 & 0 & +i\mu & 0 & +i\Delta_{p,2} & 0 & +i\nu_1 & 0 & 0 & 0 \\ 0 & 0 & 0 & -i\mu & 0 & -i\Delta_{p,2} & 0 & -i\bar{\nu}_2 & 0 & 0 \\ +i\mu & 0 & 0 & 0 & +i\nu_2 & 0 & +i\Delta_{p,2} & 0 & 0 & 0 \\ 0 & -i\mu & 0 & 0 & 0 & -i\bar{\nu}_2 & 0 & -i\Delta_{p,2} & 0 & 0 \\ 0 & 0 & 0 & 0 & 0 & 0 & 0 & 0 & 0 & 0 \\ 0 & 0 & 0 & 0 & 0 & 0 & 0 & 0 & 0 & 0 \end{bmatrix} + \begin{bmatrix} -\frac{\kappa_1}{2} & 0 & 0 & 0 & 0 & 0 & 0 & 0 & 0 & 0 \\ 0 & -\frac{\kappa_1}{2} & 0 & 0 & 0 & 0 & 0 & 0 & 0 & 0 \\ 0 & 0 & -\frac{\kappa_1}{2} & 0 & 0 & 0 & 0 & 0 & 0 & 0 \\ 0 & 0 & 0 & -\frac{\kappa_1}{2} & 0 & 0 & 0 & 0 & 0 & 0 \\ 0 & 0 & 0 & 0 & -\frac{\kappa_2}{2} & 0 & 0 & 0 & 0 & 0 \\ 0 & 0 & 0 & 0 & 0 & -\frac{\kappa_2}{2} & 0 & 0 & 0 & 0 \\ 0 & 0 & 0 & 0 & 0 & 0 & -\frac{\kappa_2}{2} & 0 & 0 & 0 \\ 0 & 0 & 0 & 0 & 0 & 0 & 0 & -\frac{\kappa_2}{2} & 0 & 0 \\ 0 & 0 & 0 & 0 & 0 & 0 & 0 & 0 & 0 & 0 \\ 0 & 0 & 0 & 0 & 0 & 0 & 0 & 0 & 0 & 0 \end{bmatrix} \quad (\text{B39})$$

microwave time-domain matrix:

equivalently $\alpha_i = 0$) using:

$$\mathbf{q}_p = M^{-1} K \mathbf{q}_{in,p}. \quad (\text{B51})$$

It should be noted, that the pump may be injected into several modes with arbitrary intensity, but we choose to inject the pump in forward (clockwise direction) only, giving a pump input vector of the form:

$$\mathbf{q}_{in,p} = \frac{P_p}{\hbar\omega_p} [1 \ 1 \ 0 \ 0 \ 0 \ 0 \ 0 \ 0 \ 0 \ 0], \quad (\text{B52})$$

with the on-chip pump power P_p . Then, we plug the values for the steady state amplitudes into the α coefficients of the full matrix, and solve the full problem.

The optical transmission and microwave reflection can then be calculated as:

$$T_{opt} = \left| \frac{a_{out,c}}{a_{in,c}} \right|^2 \quad (\text{B53})$$

$$R_{mw} = \left| \frac{b_{out}}{b_{in}} \right|^2. \quad (\text{B54})$$

The transduction efficiencies for the anti-Stokes and Stokes sidebands are defined as:

$$\eta_{AS} = \left| \frac{a_{out,c}}{b_{in}} \right|^2 \quad (\text{B55})$$

$$\eta_S = \left| \frac{a_{out,c}^\dagger}{b_{in}} \right|^2. \quad (\text{B56})$$

4. Microwave spurious mode coupling

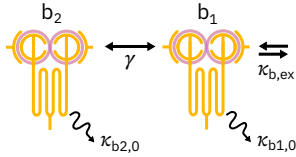


Figure 13. **Coupled microwave mode schematic.** The main microwave mode b_1 is coupled to the bus waveguide at a rate $\kappa_{b,ex}$ and is additionally coupled to a spurious mode b_2 at a rate γ . The intrinsic loss rates of the two modes are $\kappa_{b1,0}$ and $\kappa_{b2,0}$, respectively.

We now derive the linear response for the system of coupled microwave modes drawn in Fig. 13. The system comprises two microwave resonators b_1 and b_2 with resonance frequencies and intrinsic loss rates, ω_{b1} and ω_{b2} , as well as $\kappa_{b1,0}$ and $\kappa_{b2,0}$, respectively. The main microwave mode b_1 is coupled to a bus waveguide at a rate $\kappa_{b,ex}$, and is additionally coupled to the second resonance b_2 at a rate γ .

The system hamiltonian reads:

$$H = +\hbar\omega_{b,1}b_1^\dagger b_1 + \hbar\omega_{b,2}b_2^\dagger b_2 \quad (\text{B57})$$

$$+ \hbar\gamma (b_1 + b_1^\dagger) (b_2 + b_2^\dagger). \quad (\text{B58})$$

We can drop the terms rotating at twice the microwave frequency, assuming that both resonance frequencies are similar, leaving us with:

$$H = +\hbar\omega_{b,1}b_1^\dagger b_1 + \hbar\omega_{b,2}b_2^\dagger b_2 \quad (\text{B59})$$

$$+ \hbar\gamma (b_1 b_2^\dagger + b_1^\dagger b_2). \quad (\text{B60})$$

We can define the input and output vectors of the MW field:

$$\vec{q}_{in} = [b_{in} \ b_{in}^\dagger \ 0 \ 0], \quad (\text{B61})$$

and

$$\vec{q}_{out} = [b_{out} \ b_{out}^\dagger \ 0 \ 0]. \quad (\text{B62})$$

We can infer the scattering matrix elements S using Eq. B12 with the input-output matrix K :

$$K = \begin{bmatrix} \sqrt{\kappa_{b,ex}} & 0 & 0 & 0 \\ 0 & \sqrt{\kappa_{b,ex}} & 0 & 0 \\ 0 & 0 & 0 & 0 \\ 0 & 0 & 0 & 0 \end{bmatrix}, \quad (\text{B63})$$

and the time-domain dynamical matrix M' :

$$M' = \begin{bmatrix} -i\omega_{b,1} & 0 & +i\gamma & 0 \\ 0 & +i\omega_{b,1} & 0 & -i\gamma \\ +i\gamma & 0 & -i\omega_{b,2} & 0 \\ 0 & -i\gamma & 0 & +i\omega_{b,2} \end{bmatrix} \quad (\text{B64})$$

$$+ \begin{bmatrix} -\frac{\kappa_{b1,0}}{2} & 0 & 0 & 0 \\ 0 & -\frac{\kappa_{b1,0}}{2} & 0 & 0 \\ 0 & 0 & -\frac{\kappa_{b2,0}}{2} & 0 \\ 0 & 0 & 0 & -\frac{\kappa_{b2,0}}{2} \end{bmatrix}, \quad (\text{B65})$$

from which the frequency-domain dynamical matrix $M(\omega) = (-i\omega\mathbb{I} - M')$ follows as:

$$M(\omega) = \begin{bmatrix} \frac{1}{\chi_{b,1}(\omega)} & 0 & -i\gamma & 0 \\ 0 & \frac{1}{\bar{\chi}_{b,1}(-\omega)} & 0 & +i\gamma \\ -i\gamma & 0 & \frac{1}{\chi_{b,2}(\omega)} & 0 \\ 0 & +i\gamma & 0 & \frac{1}{\bar{\chi}_{b,2}(-\omega)} \end{bmatrix}. \quad (\text{B66})$$

Appendix C: Sample preparation

1. Sample fabrication

We have developed a process to fabricate low-loss, high-confinement photonic waveguides and resonators in BaTiO₃

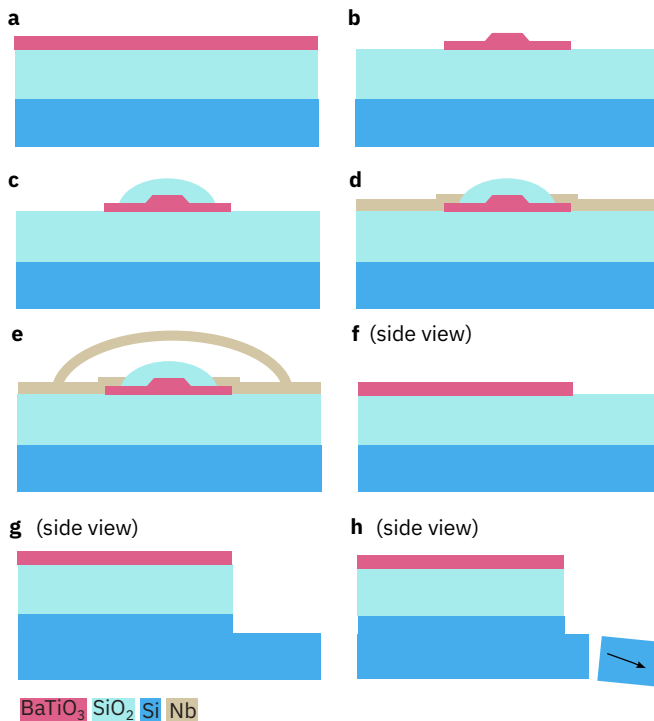


Figure 14. **Fabrication flow.** (a) initial material stack. (b) optical ridge waveguide with etched slab. (c) Oxide clad ridge waveguide. (d) Added main electrode layer. (e) Added superconducting air bridges. (f) Chip edge prior to facet fabrication. (g) Dry-etched facet. (h) Diced chip edge.

and integrate them with Nb superconducting circuits. We start with a 225-nm thick BaTiO_3 thin film bonded on $3\ \mu\text{m}$ of SiO_2 on silicon as delivered by Lumiphase AG (Fig. 14a). BaTiO_3 ridge waveguides are patterned using electron beam lithography and dry etched to produce a 100-nm thick slab and 125-nm thick ridge (b). The waveguides are protected with a $1.5\text{-}\mu\text{m}$ cladding of SiO_2 (c). Electrodes are subsequently fabricated by sputtering Nb and patterning using electron beam lithography (d). For waveguide-superconductor and superconductor-superconductor crossings, Nb airbridges are fabricated (e) by sputtering Nb and subsequent optical lithography (e). In the last step, optical facets are etched such that waveguides reach to the edge of the chip for low-loss fiber coupling (f shows a side-view of the chip before optical facet fabrication). Optical facets are fabricated using optical lithography, SiO_2 dry etching and deep reactive-ion etching into the Si substrate (g). The chip is diced to facilitate access to the facet (h).

Using this process, a variety of elements are fabricated to produce the optical and electronic circuits constituting the transducer. Fig. 15a shows a scanning electron micrograph (SEM) of a cross section of an optical ridge waveguide, Fig. 15b a close-up view of the waveguide facet, Fig. 15c the optical waveguide coupling region seen from the top, and Fig. 15d a Nb air bridge of an air-clad device. Fig. 15 depict the device under test measured in this study, with oxide-clad waveguides.

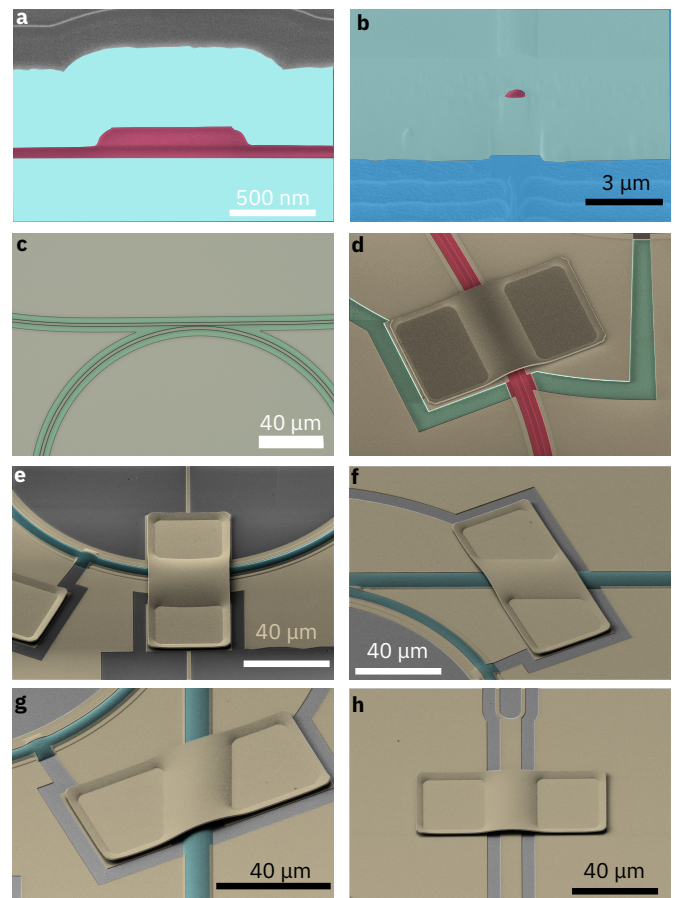


Figure 15. **Fabrication results.** False colored images scanning electron micrographs: (a) Cross-section of an oxide clad BaTiO_3 ridge waveguide. (b) Optical chip facet with BaTiO_3 taper end. (c) Optical micrograph of directional coupler section between ring and bus waveguide.

2. Packaging

In- and output high numerical aperture fibers (UHNA7, mode-field diameter $3.2\ \mu\text{m}$) are first aligned to the chip by optimizing the optical transmission through the bus waveguide. The fiber is then glued to the chip facet and subsequently glued to the package further back with additional gluing points as shown in Fig. 16.

Next, the on-chip electrical circuit is connected to the printed circuit board with wire bonds (Fig. 16). In this case, the transducer device (device 2) is fully packaged with three leads for microwave reflection, photonic molecule tuning and domain biasing. A second device (device 6) is packaged with connected microwave reflection and domain biasing port for microwave characterization.

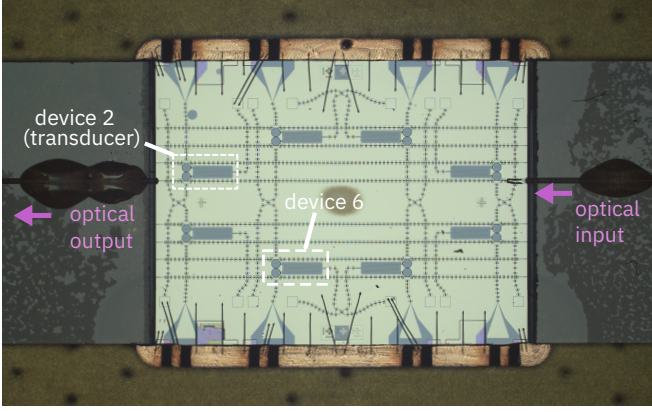


Figure 16. **Cryogenic microwave-optical co-packaged chip.** (a) Sample chip with optical edge-coupling gluing points. (b) Electrical on-chip circuit and wirebonds to printed circuit board. Lines to the inductor are highlighted in red, and to ring electrodes in yellow.

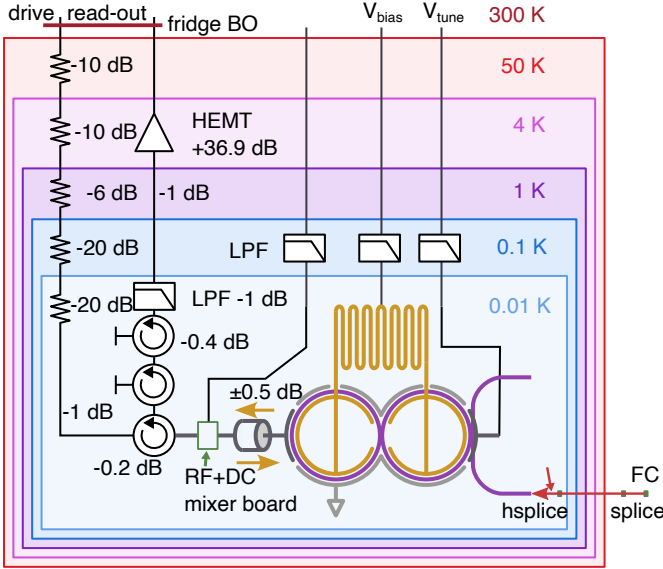


Figure 17. **Cryostat wiring with device under test.** Microwave signals are delivered to the device through the drive input at the cryostat breakout (fridge BO) via coaxial cables and a series of attenuators, a circulator and a RF+DC mixer board. The reflected microwave signal is passed through two isolators, a low pass filter (LPF) and a high electron mobility amplifier (HEMT) before being delivered to the read-out channel at the fridge breakout. Bias and tuning voltages V_{bias} and V_{tune} , respectively, are delivered to the device via twisted wire pairs through low pass filters (LPF). Optical signals are delivered through a fiber going from room temperature into the bottom probe of the cryostat, which is spliced to the packaged device fiber before sample mounting.

Appendix D: Experimental setups

1. Cryostat wiring

The wiring inside the cryostat is shown in Fig. 17. Our cryostat (BlueFors LD400) features a fast sample exchange

bottom probe mechanism. While the electrical signals are delivered from the top of the cryostat at the cryostat breakout connectors (fridge BO), the optical fiber is fed through the bottom probe to the device.

For microwave drive signal delivery, SCuNi-CuNi semi rigid coaxial cables lead from the breakout connectors at the top down to the mixing chamber plate of the cryostat. They are attenuated at the different stages according to the temperature gradient to the previous stage (i.e. from 4 to 1 K) only -6 dB while from 1 to 100 mK by -20 dB. At the mixing chamber plate a circulator is connected which in turn passes the signals through a custom mixer board for the ability to combine microwave and direct current (dc) electrical signals up to ± 30 V. The reflected microwave signal is sent through two isolators via the circulator, which, importantly, are all thermalized to the mixing chamber plate. The signal is then filtered with a low pass filter and delivered to a high electron mobility amplifier (HEMT) at the 4 K stage via NbTi superconducting coaxial cables, which are thermalized to each stage with 0 dB attenuators. To avoid bulky fiber connectors, the high numerical aperture fibers (UHNA7) of the packaged sample are spliced to the standard single mode fibers (SMF-28) using a hybrid splicing program that creates a smooth transition between the two (hssplice), with typical losses on the order of -1 dB. A second standard splice between two SMF-28 fibers connects the cryostat fiber to the fiber connector (FC).

2. Pulsed microwave characterization

To characterize the microwave reflection under pulsed optical pumping, we use a setup very similar to the pulsed transduction setup. The main difference is, that only the pump laser is sent to the device, and instead of measuring the transduced signal, we measure the high power microwave reflection from the device. This means, that only the pulse power sum measurement with the monitoring diode is necessary. Due to the high microwave probe power levels, we remove the room temperature amplifier from the detection chain (RT read amp line). The measurement and pulse sequence is virtually identical to the pulsed transduction measurement described in Sec. D4. Time resolved microwave spectra are recorded by running the full sequence for each frequency step. For time efficiency, only a narrow frequency span of a few MHz because the main parameters of interest are the extinction and frequency shift. To calculate the extinction, a larger span measurement is taken once using the same routine and setup to obtain the required reference level. Note, that the setup is readily converted to the pulsed transduction configuration, which can be used to monitor the fiber-to-chip coupling efficiency between experiments.

3. Continuous wave transduction

The setup for continuous wave and bidirectional transduction measurements is shown in Fig. 19. Two continuously tunable external-cavity diode lasers (Laser 1 and 2) are used

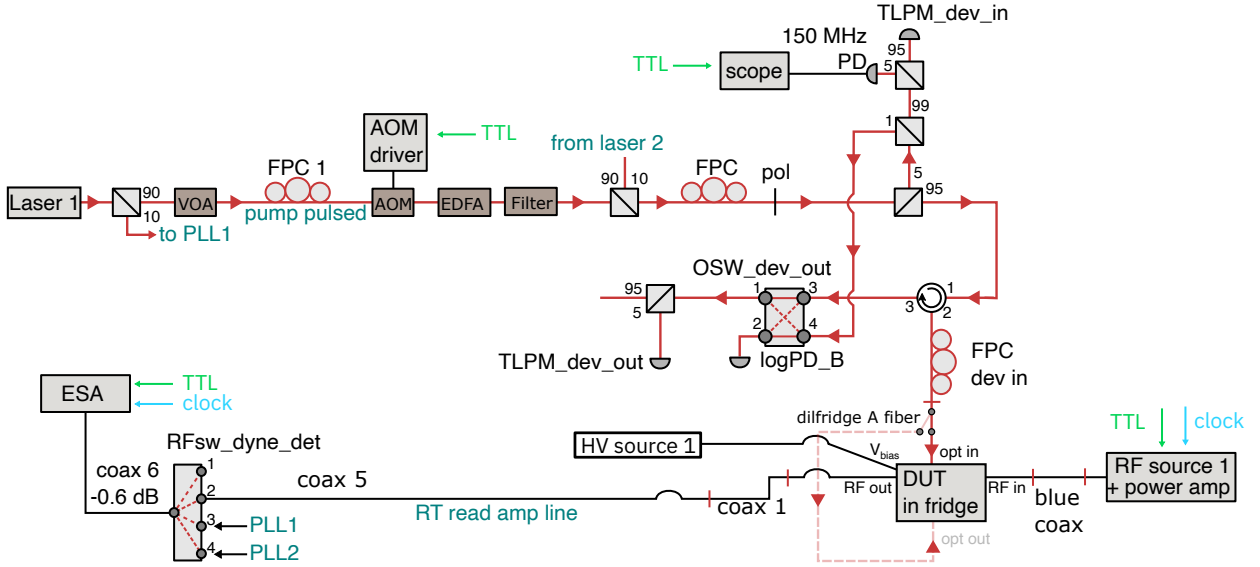


Figure 18. Pulsed microwave characterization setup.

for optical pumping and probing. The main and pump laser in the cw experiment is Laser 2. A portion of the light from Laser 2 is sent to the frequency referencing path, where a coarse Mach-Zehnder interferometer (MZI) with a free spectral range of about 2.5 GHz is used to monitor laser detuning sweeps during transduction measurements. Another fraction of the light is sent as local oscillator (LO) to the heterodyne detection setup. Next, a fraction of light is combined with that of the auxiliary laser Laser 1 to generate the optical beating to offset-lock Laser 1 with a defined frequency offset to Laser 2 using a phase-locked loop (PLL). Here, only the pulsed laser paths were used. Both lasers are polarization controlled using a fiber polarization controller (FPC) to maximize the transmitted power through the acousto-optic modulators (AOM) while minimizing laser frequency dependent power variations, and then sent to variable optical attenuators (VOA) to adjust their power levels. Both lasers are combined on a 50/50 splitter before which Laser 2's polarization is again optimized using an FPC to align both laser polarizations. After passing through an optical switch (OSW_dev_in), the polarization of the light is optimized to maximize the transmission through the electro-optic modulator (EOM). A polarization filter (pol) behind the EOM ensures equal polarization for both lasers. The 150 MHz photodiode (PD) and fiber-stretcher (FS) were not actively used in this experiment. A fraction of the light is sent to a power meter (TLPM_dev_in) to monitor the power sent to the cryostat. The light passes through a circulator and is sent to the device via a final FPC. Light reflected from the cryostat fiber is sent to switch OSW_dev_out to either monitor the device reflection on the logarithmic photodiode (logPD_B) or to the heterodyne detection path. For calibration purposes, the laser signal can be sent into FPC dev in to directly be sent to the detection path. In the heterodyne detection path, the reflected power is monitored with power meter TLPM_dev_out and the polarization optimized using FPC dev return to optimize the overlap with the local oscillator. The light is then

combined with the local oscillator and detected on the GHz photodiode RX10.

Electrical input signals are generated using a radiofrequency source (RF source 1) and the heterodyne transduction signal is detected on an electronic spectrum analyzer (ESA). Optical input signals generated either as a single sideband from offset-locking Laser 2 to Laser 1 (PLL), or by modulating the EOM using the vector network analyzer (VNA). The electrical signals from the cryostat are sent through the read out amplification line (RT read amp line) and detected either on the ESA or the VNA.

Note, that the phase-lock (PLL1), Laser 2's AOM source, RF source 1 and the ESA are phase locked to a 10 MHz reference clock. This allows the lowest possible noise during electrical detection with the ESA. Since we only had one referenced AOM source, the AOM for Laser 1 is free running with a systematic offset of a few kHz from the nominal 110 MHz of both AOMs. This slight offset is beneficial for the electrical detection of the optical-to-microwave signal on the ESA, as the PLL reference signal creates spurious noise. This means, driving Laser 1's AOM with the same AOM source would lead to additional detection noise. Ideally in the future, Laser 1's AOM should be driven by a source with clock input but at a slight frequency offset to Laser 2's AOM. This noise issue does not exist for the microwave-to-optical direction, as the detected heterodyne signal is shifted by the AOM frequency (110 MHz).

4. Pulsed transduction

For studying the system in pulsed operation, we only perform optical-to-microwave transduction using two lasers with an offset lock, as the signal is less sensitive to variations in the optical reflection from the device compared to the microwave-to-optical signal. The setup is shown in Fig. 20 and is a vari-

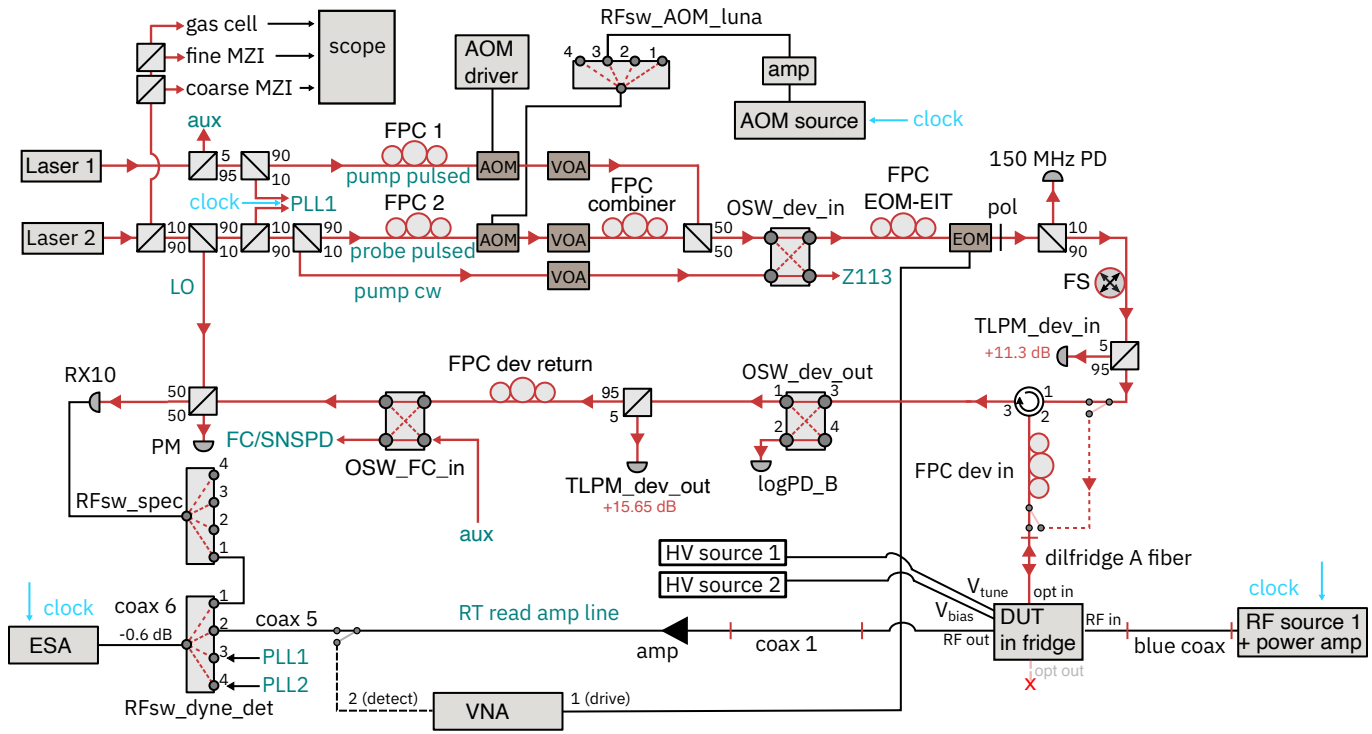


Figure 19. Continuous wave transduction setup.

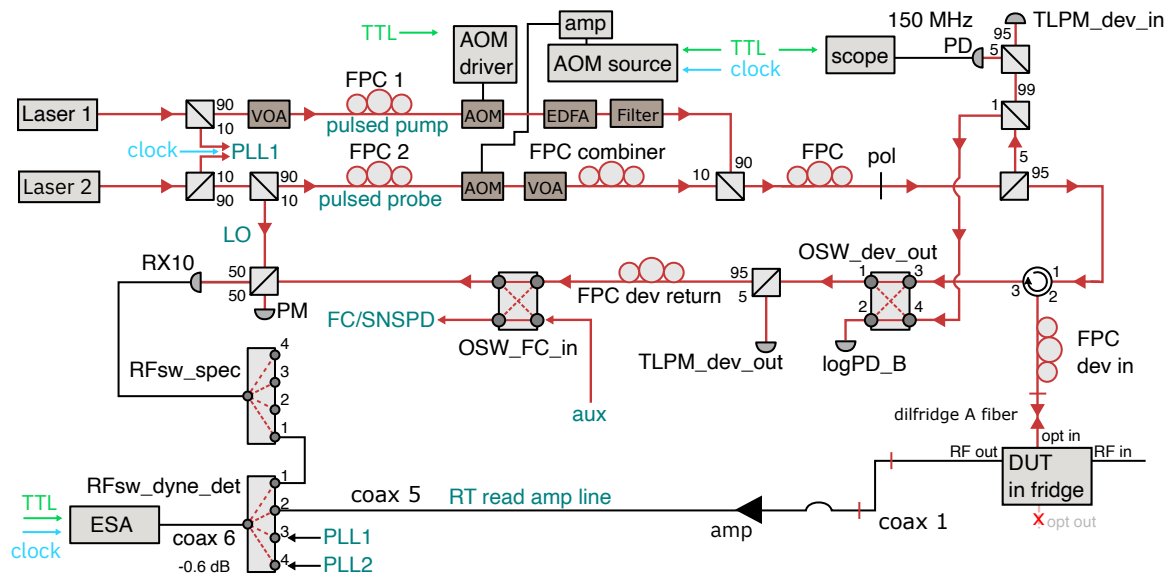


Figure 20. Pulsed transduction setup.

ation of the continuous wave setup discussed previously. It differs, however, in certain important points which are mainly related to the generation and monitoring of high power pump pulses.

In this configuration, Laser 2 is the signal laser whose AOM is now pulsed using a transistor-transistor-logic (TTL) signal from a pulse generator. To achieve large peak powers, the pulsed optical signal of Laser 1, which now acts as the pump, is amplified using an erbium-doped fiber amplifier (EDFA) whose amplified spontaneous emission noise (ASE) is filtered using a tunable filter. Both laser are then combined, but now using a 90/10 splitter to maximize the pump pulse power. The combined lasers are again sent through a polarization controller and filter.

Due to the large power range that needs to be covered, the power monitoring had to be modified. To that end, a portion of the light is sent to a pulse monitoring branch, where the standard power meter measures the average power (TLPM_dev_in), while a fast photodiode (bandwidth 150 MHz) is used to monitor the optical pulse shape on an oscilloscope, representing the sum of both lasers. Another fraction of the light is sent to the heterodyne detection arm, which we now use to monitor the power ratio of the optical pulses. Due to the frequency offset between the two, this detection method also enables recording the pulse shape of each individual pulse with superior signal-to-noise compared to the sum monitoring diode.

Using an electrical switch (RFsw_dyne_det) either the optical pulse shapes and ratios are monitored using the heterodyne signal, or the transduction signal from the room temperature (RT) read-out amplification line is measured using an electronic spectrum analyzer (ESA).

Appendix E: Optical and direct current characterization

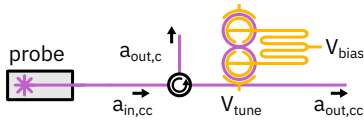


Figure 21. **Optical characterization measurement schematic.** Light is injected via the counter clockwise input mode $a_{in,cc}$ and the transmission to $a_{out,cc}$ or reflection to $a_{out,c}$ is measured.

1. Room temperature transmission before cooldown

In this section, the optical response of the device is studied in transmission at room temperature before cooldown, as shown in Fig. 21. The transmission coefficient in this case is defined as $T = |a_{out,cc}/a_{in,cc}|^2$. Note, that for all measurements shown in this section no voltage was applied to the device.

We apply the photonic molecule with backscattering fit model to each resonance in the spectrum and plot the resulting

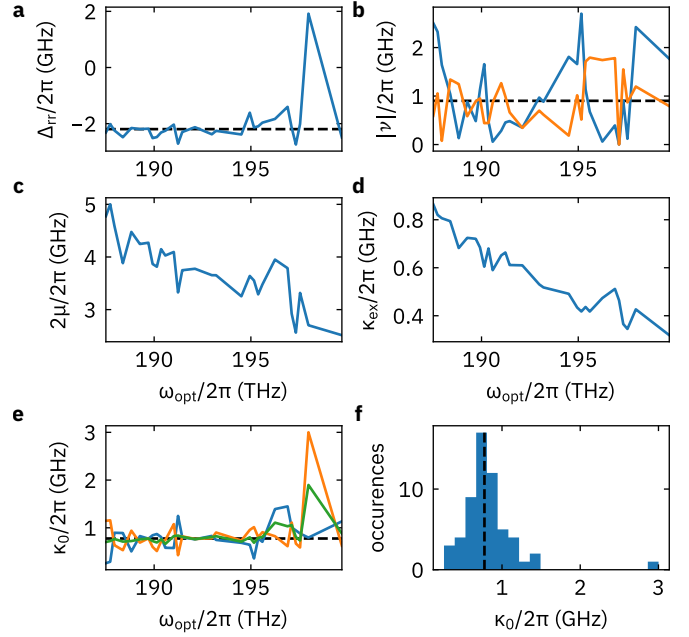


Figure 22. **Detuning and loss and coupling rates vs. optical frequency.** (a) Ring-ring detuning and (b) back scattering rates as a function of optical frequency. (c) Resonant ring-ring and (d) external bus coupling rate as a function of optical frequency. (e) Intrinsic loss rates as a function of optical frequency (e) and their distribution (f). Fit results of transducer (device 2) optical spectrum. When more than one trace is shown, blue represents the result for the first ring, orange for the second, and green the average of the two. The dashed lines show average ring-ring detuning $\bar{\Delta}_{rr}/2\pi = -2.2$ GHz, intrinsic loss rate $\bar{\kappa}_{a,0}/2\pi = 776$ MHz and back-scattering amplitude $|\bar{\nu}|/2\pi = 902$ MHz.

detuning and rates as a function of optical frequency (Fig. 22). Apart from a single outlier at high optical frequencies, the detuning between the rings Δ_{rr} seems to be consistently around -2.2 GHz (Fig. 22a). Note, that no bias or tuning voltage have been applied to the device at that point. The resonant Rabi splitting $\hbar\Omega = 2\mu$ (Fig. 22b) shows the expected reduction with optical frequency, and reaches almost 5 GHz at the longest wavelengths (lowest frequencies). The intrinsic loss rates (Fig. 22c) are scattered around 776 MHz, where, as previously mentioned, the average value of the two rings (green trace) seems to be more reliable than the individual ring loss rates. The forward backward coupling amplitudes (Fig. 22d) scatter quite a log with no discernible regularity, which is consistent with randomly distributed scattering defects along the ring. The external bus coupling rate also shows the expected dispersion with more than 800 MHz at the lowest frequencies. The distribution of intrinsic loss rates is peaked around the mean value indicating a reliable fit with the exception of the outlier at 3 GHz which corresponds to the previously mentioned outlier at large frequencies.

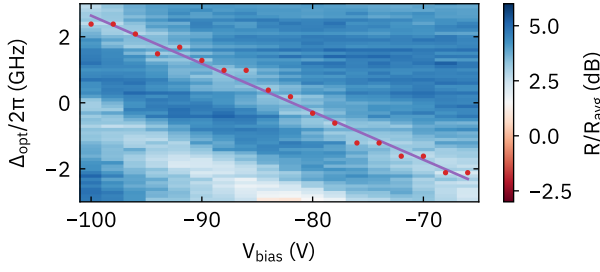


Figure 23. **Cryogenic electro-optic tuning efficiency.** Linear fit to the V_{bias} tuning dependence of the optical resonance frequency around the standard working point $V_{\text{bias}} = -100$ V. The extracted slope is $\partial\omega_a/\partial V = 2\pi \cdot 145$ MHz V^{-1} .

2. Cryogenic temperature optical tuning

Next, we extract the resonance frequency ω_a of the photonic molecule as a function of bias voltage in the linear range close to the standard working point of $V_{\text{bias}} = -100$ V (Fig. 23). We then fit a linear function to the trend, and extract an electro optic tuning efficiency of $\partial\omega_a/\partial V = 2\pi \cdot 145$ MHz V^{-1} . This value can later be used to estimate the vacuum coupling strength, as the DC-tunability is typically an upper bound for that in the microwave domain.

3. Room temperature optical transmission after cooldown

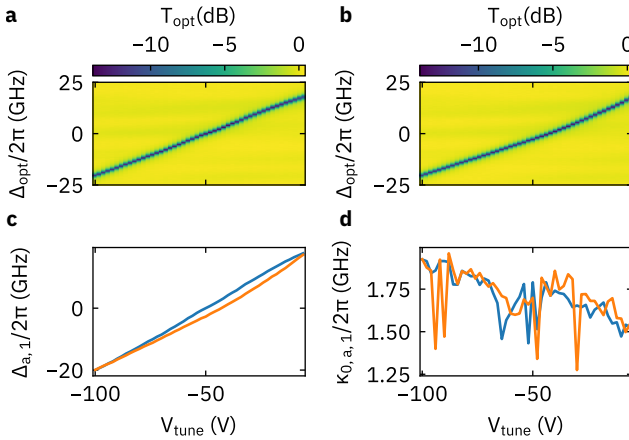


Figure 24. **Post-cooldown room temperature tuning hysteresis and loss.** Optical transmission for a (a) down- and (b) up-sweep of the tuning voltage. (c) Optical resonance frequency tuning and (d) intrinsic optical loss rate as a function of tuning voltage for up (orange) and down (blue) sweep.

Since no voltages were applied to the transducer device prior to cooling down the sample, we characterize the sample post-cooldown at room temperature. Interestingly, the response (Fig. 24) looks vastly different to the expected ferroelectric response of BaTiO_3 at room temperature [39]. While we do not have experimental characterization of this exact device prior to cooldown, other devices fabricated in this plat-

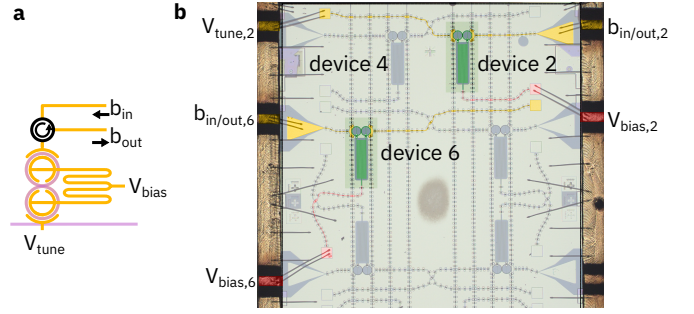


Figure 25. **Microwave characterization measurement schematic.** (a) A microwave tone is injected in b_{in} , reflected at the device and is sent to b_{out} via a circulator. (b) Optical micrograph of the two electrically packaged devices (device 2, device 6).

form have shown the expected quadratic-like behavior at room temperature. Therefore, we suspect that the material was permanently altered compared to before cooldown. Judging from the fact that the polarity of the tuning is inverted, one may conclude that the ferroelectric domains have a permanent preferential orientation after cooldown. This may be due to the fact, that the device was usually biased to $V_{\text{bias}} = -100$ V during most cryogenic measurements. While the voltage is brought back to ground before warmup, the domains may still have been oriented and kept their orientation during warmup.

When looking at the optical resonance tuning in the negative branch only (between 0 and -100 V), we note that the response is nearly free of hysteresis (Fig. 24c) when comparing the up- and downsweeps. The dc-tuning efficiency is about $\partial\omega_a/\partial V = 2\pi \cdot 395$ MHz. Interestingly, the average intrinsic loss rate (averaged over optical frequency) has increased by about a factor of two compared to the initial room temperature characterization prior to application of dc-voltages and before cooldown (Fig. 22). Furthermore, there seems to be an increase in optical loss rate as a function of tuning voltage as shown in Fig. 24d.

Appendix F: Microwave characterization

In this section, the continuous wave microwave response of the device is studied in reflection as shown in Fig. 25. The reflection coefficient in this case is defined as $R = |b_{\text{out}}/b_{\text{in}}|^2$.

1. Bias dependence

Analogously to the characterization of the optical response as a function of bias voltage, we now study the microwave reflection with applied bias. While only one device (device 2) is fully packaged, we wired up a reference device (device 6) for microwave characterization. The microwave reflection as a function of bias voltage of both devices is shown in Fig. 26. The first thing to note is, that the response shows a significant bias dependence. Unfortunately, the main transducer device (device 2, Fig. 26b) exhibits an anticrossing to an unknown

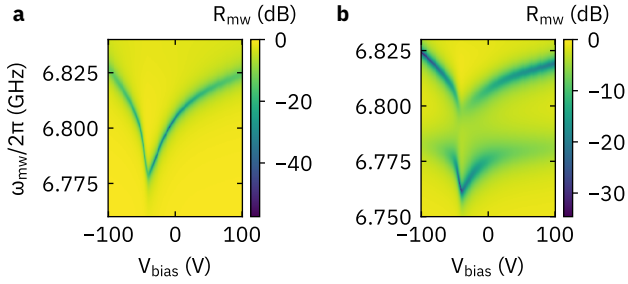


Figure 26. **Microwave reflection vs. bias voltage.** (a) Device 6 and (b) device 2 microwave reflection vs. bias voltage V_{bias} .

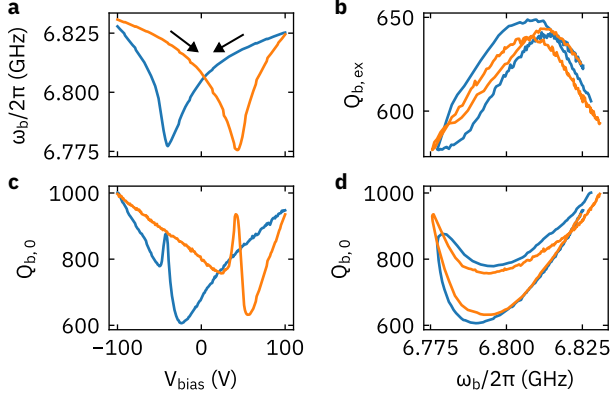


Figure 27. **Bias dependence of microwave properties: device 6.** (a) Microwave resonance frequency ω_b and (b) intrinsic quality factor $Q_{b,0}$ as a function of bias voltage V_{bias} . (c) External quality factor $Q_{b,\text{ex}}$ and (d) intrinsic quality factor $Q_{b,0}$ as a function of microwave resonance frequency ω_b .

spurious mode at around 6.79 GHz. The observed resonant interaction splitting is $2\gamma = 2\pi \cdot 31.9$ MHz.

For characterization of general microwave parameters, we initially focus on device 6 (Fig. 26a) for a simplified model description with less error sources and fit parameters than the actual transducer device with spurious mode coupling requires. To that end, we take a full hysteresis curve and fit a single resonance model (NLQFIT7) to the data using the python package scikit-rf [59]. Fig. 27a shows the bias dependence of the microwave resonance frequency, revealing a almost perfectly symmetric hysteresis curve as expected for a ferroelectric material. Note that, apart from the asymmetry and noise, the microwave hysteresis of device 6 shows a qualitatively similar shape to that of device 2 (2h). Importantly, the coercive field values align well. The bias dependence can most likely be attributed to a bias dependent microwave permittivity of the material, making it a nonlinear capacitor. Interestingly, the intrinsic quality factor also depends on the applied bias (Fig. 27b). Generally, bias voltages beyond the coercive field seem to lead to higher quality factors, with the minimal quality factor reached for values close to the coercive field. Right at the coercive field however, a local peak in the quality factor is observed. While this behavior may be explained by a bias dependent material absorption of microwave radiation, it may also stem from piezoelectric actuation, since

| | |
|-----------------------------|---|
| $\omega_{b,2}/2\pi$ | 6.792 GHz |
| $\kappa_{b2,0}/2\pi$ | 11.4 MHz |
| $\gamma/2\pi$ | 15.95 MHz |
| ref. level | $ S ^2$ @ 6.835 GHz, $-100 V_{\text{bias}}$ |
| $\kappa_{b,\text{ex}}/2\pi$ | 7 MHz |

Table III. **Effective dc-tuning model parameters.** The parameters listed here were fixed when fitting the reflection of device 2. $\kappa_{b,\text{ex}}$ was only fixed for experiments where the resonance frequency did not shift significantly, that is for microwave power dependence and optical power dependence measurements. For the temperature and bias dependence it is a free fit parameter.

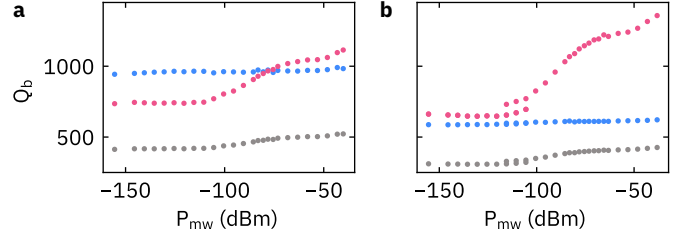


Figure 28. **Microwave quality factor vs. microwave power.** (a,b) External (blue), loaded (grey) and intrinsic microwave quality factor for device 2 and 6, respectively, as a function of microwave power P_{mw} . The bias voltage for both measurements is $V_{\text{bias}} = -100$ V.

it is known that most electro-optic materials also feature a non-zero piezo-electric effect. Right at the coercive field, one would expect the ferroelectric domains to have a net vanishing polarization, which would explain the local peaks of the microwave quality factor. The fact that the largest microwave loss is observed close to the net zero polarization point suggests, that the piezoelectric coupling may be largest there. For completeness, the external microwave coupling quality factor is plotted versus frequency (Fig. 27c) and shows a slight frequency dependence, which may stem from reflections in the bus line.

In order to extract the bias dependence of the bare transducer resonance frequency of device 2, we use the coupled microwave mode model derived in Appendix B 4. Since a fit of the complex S-parameter response is involved, we implement a fit of the magnitude $|S|$. To improve the fit stability, we fix certain parameters as listed in Table III.

2. Microwave power dependence

So far, we have been probing the microwave system in the medium to high power regime. Typically however, the signal levels in transducers for quantum transduction are just a few or even single photons. In this low power regime, absorption from two-level systems may become a significant loss channel, as the circulating power is no longer sufficient to saturate the two-level systems in the dielectric for example. For this reason, we probe the microwave reflection of device as a function of incident microwave power. By fitting the microwave response of device 2 and 6 as a function of microwave probe power, again using the single resonance model

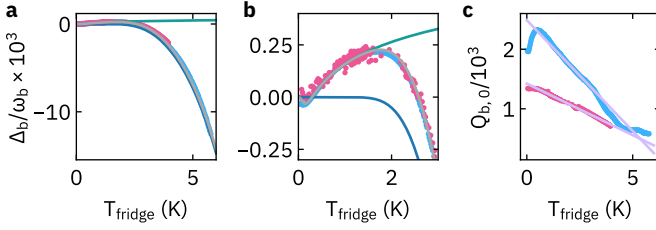


Figure 29. **Microwave resonance shift and quality factor vs. temperature.** (a) Full and (b) reduced temperature range plot of relative resonance frequency shift Δ_b/ω_b and intrinsic microwave quality factor $Q_{b,0}$ as a function of cryostat temperature T_{fridge} for (c) device 6 and (d) device 2, respectively.

NLQFIT7 from the scikit-rf package [59], we can extract the external and intrinsic quality factors $Q_{b,\text{ex}}$ and $Q_{b,0}$, respectively. As expected, the external coupling quality factor is independent of microwave power. Interestingly, it is different between both devices, with 960 and 605 for device 2 and 6, respectively. This potentially be attributed to the fact, that the transmission lines from the wire bonding pads to the devices have different lengths (see Fig. 25b). While device 6 has a very short line without optical crossings, the transmission line of device 2 has two optical crossings and is longer. The low power quality factors are 740 and 650 for device 2 and 6, respectively.

3. Temperature dependence

In this section, we sweep the temperature of the cryostat ("fridge") by either evaporating the helium cooling mixture (warm up) or recondensing it (cool down) while simultaneously measuring the microwave reflection at high probe power. Note, that this means that both the bottom probe and mixing chamber temperature are swept simultaneously, which we call T_{fridge} .

In a first analysis step, we extract the observed center frequency of the reflection dip and its extinction as a function of temperature for both devices. While for device 6 the observed reflection dip frequency corresponds to the actual bare resonator frequency ($\omega'_b = \omega_b$), the observed frequency of device 2 is shifted due to coupling to the spurious mode. We therefore need to fit the response with the two-mode model to extract the bare frequency.

To further quantify the observed frequency shift and loss rate, we fit the spectra to extract the resonance frequency shift and quality factor change as a function of temperature. For device 6 we again use the simple resonance fit NLQFIT7 of the scikit-rf python package [59]. For device 2 we use the more complex model that takes into account the coupling to the spurious mode (see Appendix B 4). The fixed fit parameters are listed in Table III. The resulting relative frequency shift and intrinsic quality factor as a function of temperature are plotted in 29 in blue and magenta for device 2 and 6, respectively. As shown in Fig. 29b, the relative frequency shift is almost identical for both devices. For both devices, the intrinsic quality

| $Q_{b,0,\text{TLS}}$ | T_C | α |
|----------------------|-------|----------|
| 2038 | 8.7 K | 7.8 % |

Table IV. **Thermal microwave frequency shift fit parameters.** Fit results for free parameters from equations F1, F2 and F3 fitted to the data shown in Fig. 29a and b.

factors decrease monotonously as a function of temperature for $T_{\text{fridge}} > 0.6 \text{ K}$. Note, that the quality factor for device 6 only depends on the loaded linewidth and observed extinction, and should therefore be accurate. The additional spurious mode for device 2 introduces additional parameters such as the loss and coupling rate of the spurious mode which cannot be unambiguously separated, meaning that the extracted intrinsic quality factor shown here for device 2 may have a large systematic error.

While the red-shift and decrease of intrinsic quality factor are a typical signature of quasiparticle (QP) generation in the superconductor, the initial blue shift has been attributed to two-level systems (TLS) often present in dielectrics with defects or amorphous composition [47, 48]. The observed relative frequency shift is then described as a sum of both effects [48]:

$$\frac{\Delta\omega_b}{\omega_b} = \left(\frac{\Delta\omega_b}{\omega_b}\right)_{\text{TLS}} + \left(\frac{\Delta\omega_b}{\omega_b}\right)_{\text{QP}}. \quad (\text{F1})$$

The individual contributions can be modeled as [60]:

$$\left(\frac{\Delta\omega_b}{\omega_b}\right)_{\text{TLS}} = \frac{1}{\pi Q_{b,0,\text{TLS}}} \cdot \text{Re} \left\{ \Psi \left(\frac{1}{2} + i \frac{\hbar\omega_b}{2\pi k_b T} \right) - \ln \left(\frac{\hbar\omega_b}{2\pi k_b T} \right) \right\}, \quad (\text{F2})$$

with the complex digamma function Ψ , and

$$\left(\frac{\Delta\omega_b}{\omega_b}\right)_{\text{QP}} = -\frac{\alpha}{2} \left(\frac{\sin(\gamma\phi(T))}{\sin(\gamma\pi)} \left| \frac{\sigma(T)/2}{\sigma(0)} \right|^\gamma - 1 \right), \quad (\text{F3})$$

with the kinetic inductance fraction $\alpha = L_k / (L_g + L_k)$ and the kinetic and geometric inductance of the circuit L_k and L_g , respectively. The kinetic inductance of a thin superconducting film of length l is related to the complex conductivity $\sigma = \sigma_1 - i\sigma_2$ via $L_k \approx l / (wt\omega_b\sigma_2)$ for $R \rightarrow 0$ with the conductor width w and thickness t . For the conductivity, we used the expressions defined in [48].

We fit the the model to the data of device 2 and plot the TLS, QP and sum of both contributions in green, dark blue and grey, respectively (Fig. 29a,b). The fit parameters and results are listed in Table IV. We note, that the zero-temperature TLS intrinsic quality factor aligns well with the observed quality factor drop in Fig. 29c towards low temperatures, and the critical temperature is also in line with previous experimental studies on the material [61].

Additionally, linear fits of the extracted internal quality factors between 0.6 and 6 K are shown in Fig. 29c in light purple.

Appendix G: Transduction

While it was not possible to directly measure the optical response of the system during cooldown in this study, we can make use of the transduced signal to characterize the optical system. To that end, we perform an optical-to-microwave measurement as a function of tuning voltage V_{tune} , which detunes the two rings with respect to each other. As shown in Fig. 30a, the response changes significantly as a function of tuning voltage. For $V_{\text{tune}} = 100$ V, the maximum detected signal is highest (Fig. 30c) and the doubly-resonant satellite peaks are of similar height (Fig. 30b, yellow trace). This suggests, that this is the case where the rings are resonant with each other. The slight splitting of the triply resonant central peak can either arise from forward-backward scattering, or from a mismatch between microwave frequency and the optical splitting. The frequency mismatch is the more likely explanation, as otherwise the doubly-resonant peaks should also show a splitting. In the detuned case (Fig. 30b, purple trace), the maximum signal is lower as expected, but now a total of four peaks are clearly visible, indicating strong forward-backward coupling. Note, that the forward-backward coupling strength is strongly frequency dependent, and may be lower in the resonant case.

Appendix H: Slow optical heating

To characterize the slow thermalization rate in the system, we send a $10\ \mu\text{s}$ pulse of off-resonant light with a low repetition rate to the device (Fig. 31). In addition to the fast responding red-shift, which we attribute to quasiparticle generation in the case of off-resonant light, we observe a slow blue-shift and decrease in extinction, indicating heating of the dielectric. After the pulse, the system recovers to its pre-pulse state after several tens to hundreds of microseconds (Fig. 31a), which is significantly more slowly than the on-resonant dielectric and quasiparticle heating. We attribute this thermalization rate to the thermalization between the sample package and probe with the cryostat mixing chamber stage.

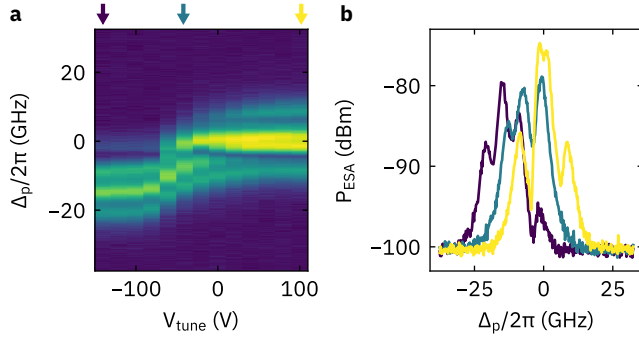


Figure 30. **Optical-to-microwave transduction vs. tuning voltage.** (a) Detected microwave-optical signal power as a function of tuning voltage V_{tune} and pump detuning Δ_p . (b) Transduction spectra for selected tuning voltages as marked with the colored arrows in a.

| Parameter | Value |
|-----------------------------|----------|
| $\Delta_{\text{rr}}/2\pi$ | 0.4 GHz |
| $\omega_b/2\pi$ | 6.82 GHz |
| $2\mu/2\pi$ | 4.7 GHz |
| $ \nu_1 /2\pi$ | 0.35 GHz |
| $\arg \nu_1$ | 0 |
| $ \nu_2 /2\pi$ | 0.15 GHz |
| $\arg \nu_2$ | 0 |
| $\kappa_{a,0}/2\pi$ | 2 GHz |
| $\kappa_{a,\text{ex}}/2\pi$ | 0.85 GHz |
| $\kappa_{b,0}/2\pi$ | 10 MHz |
| $\kappa_{b,\text{ex}}/2\pi$ | 7 MHz |
| $g_0/2\pi$ | 406 Hz |
| P_p | -10 dBm |
| $\eta_{\text{fiber2chip}}$ | -5 dB |

Table V. **System Parameters for transduction model.**

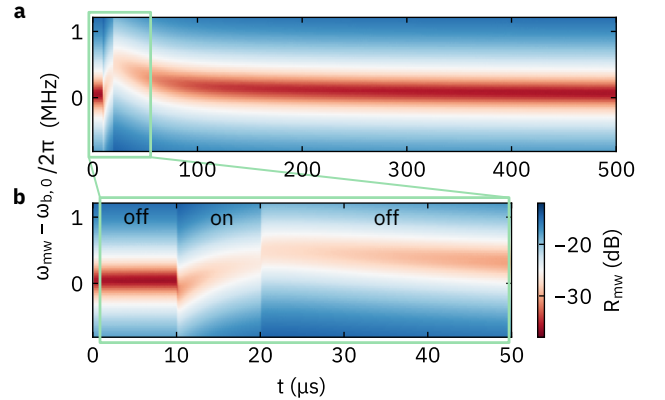


Figure 31. **Slow microwave heating under pulsed operation.** (a) Microwave reflection as a function of time and microwave probe frequency ω_{mw} around the pre-pulse dip frequency $\omega_{b,0}$. (b) Close-up of the first $50\ \mu\text{s}$ of a.

- [1] Committee on Technical Assessment of the Feasibility and Implications of Quantum Computing, Computer Science and Telecommunications Board, Intelligence Community Studies Board, Division on Engineering and Physical Sciences, and National Academies of Sciences, Engineering, and Medicine, *Quantum Computing: Progress and Prospects*, edited by E. Grumbling and M. Horowitz (National Academies Press, Washington, D.C., 2019) pages: 25196.
- [2] S. Bravyi, O. Dial, J. M. Gambetta, D. Gil, and Z. Nazario, The future of quantum computing with superconducting qubits, *Journal of Applied Physics* **132**, 160902 (2022).
- [3] P. Magnard, S. Storz, P. Kurpiers, J. Schär, F. Marxer, J. Lütolf, T. Walter, J.-C. Besse, M. Gabureac, K. Reuer, A. Akin, B. Royer, A. Blais, and A. Wallraff, Microwave Quantum Link between Superconducting Circuits Housed in Spatially Separated Cryogenic Systems, *Physical Review Letters* **125**, 260502 (2020).
- [4] A. J. Stolck, K. L. van der Eenden, M.-C. Slater, I. te Raa-Derckx, P. Botma, J. van Rantwijk, J. J. B. Biemond, R. A. J. Hagen, R. W. Herfst, W. D. Koek, A. J. H. Meskers, R. Vollmer, E. J. van Zwert, M. Markham, A. M. Edmonds, J. F. Geus, F. Elsen, B. Jungbluth, C. Haefner, C. Tresp, J. Stuhler, S. Ritter, and R. Hanson, Metropolitan-scale heralded entanglement of solid-state qubits, *Science Advances* **10**, eadp6442 (2024), publisher: American Association for the Advancement of Science.
- [5] J.-L. Liu, X.-Y. Luo, Y. Yu, C.-Y. Wang, B. Wang, Y. Hu, J. Li, M.-Y. Zheng, B. Yao, Z. Yan, D. Teng, J.-W. Jiang, X.-B. Liu, X.-P. Xie, J. Zhang, Q.-H. Mao, X. Jiang, Q. Zhang, X.-H. Bao, and J.-W. Pan, Creation of memory-memory entanglement in a metropolitan quantum network, *Nature* **629**, 579 (2024), publisher: Nature Publishing Group.
- [6] J.-G. Ren, P. Xu, H.-L. Yong, L. Zhang, S.-K. Liao, J. Yin, W.-Y. Liu, W.-Q. Cai, M. Yang, L. Li, K.-X. Yang, X. Han, Y.-Q. Yao, J. Li, H.-Y. Wu, S. Wan, L. Liu, D.-Q. Liu, Y.-W. Kuang, Z.-P. He, P. Shang, C. Guo, R.-H. Zheng, K. Tian, Z.-C. Zhu, N.-L. Liu, C.-Y. Lu, R. Shu, Y.-A. Chen, C.-Z. Peng, J.-Y. Wang, and J.-W. Pan, Ground-to-satellite quantum teleportation, *Nature* **549**, 70 (2017).
- [7] Y. Huang, F. Salces-Carcoba, R. X. Adhikari, A. H. Safavi-Naeini, and L. Jiang, Vacuum Beam Guide for Large Scale Quantum Networks, *Physical Review Letters* **133**, 020801 (2024).
- [8] D. Lago-Rivera, S. Grandi, J. V. Rakonjac, A. Seri, and H. de Riedmatten, Telecom-heralded entanglement between multimode solid-state quantum memories, *Nature* **594**, 37 (2021), publisher: Nature Publishing Group.
- [9] T. van Leent, M. Bock, F. Fertig, R. Garthoff, S. Eppelt, Y. Zhou, P. Malik, M. Seubert, T. Bauer, W. Rosenfeld, W. Zhang, C. Becher, and H. Weinfurter, Entangling single atoms over 33 km telecom fibre, *Nature* **607**, 69 (2022), publisher: Nature Publishing Group.
- [10] C. M. Knaut, A. Suleymanzade, Y.-C. Wei, D. R. Assumpcao, P.-J. Stas, Y. Q. Huan, B. Machielse, E. N. Knall, M. Suttula, G. Baranes, N. Sinclair, C. De-Eknamkul, D. S. Levonian, M. K. Bhaskar, H. Park, M. Lončar, and M. D. Lukin, Entanglement of nanophotonic quantum memory nodes in a telecom network, *Nature* **629**, 573 (2024), publisher: Nature Publishing Group.
- [11] H. J. Kimble, The quantum internet, *Nature* **453**, 1023 (2008), number: 7198 Publisher: Nature Publishing Group.
- [12] S. Wehner, D. Elkouss, and R. Hanson, Quantum internet: A vision for the road ahead, *Science* **362**, eaam9288 (2018), publisher: American Association for the Advancement of Science.
- [13] Y. Chu and S. Gröblacher, A perspective on hybrid quantum opto- and electromechanical systems, *Applied Physics Letters* **117**, 150503 (2020).
- [14] N. Lauk, N. Sinclair, S. Barzanjeh, J. P. Covey, M. Saffman, M. Spiropulu, and C. Simon, Perspectives on quantum transduction, *Quantum Science and Technology* **5**, 020501 (2020).
- [15] S. Krastanov, H. Raniwala, J. Holzgrafe, K. Jacobs, M. Lončar, M. J. Reagor, and D. R. Englund, Optically Heralded Entanglement of Superconducting Systems in Quantum Networks, *Physical Review Letters* **127**, 040503 (2021).
- [16] M. Mirhosseini, A. Sipahigil, M. Kalaei, and O. Painter, Superconducting qubit to optical photon transduction, *Nature* **588**, 599 (2020), bandiera_abtest: a Cg_type: Nature Research Journals Number: 7839 Primary_atype: Research Publisher: Nature Publishing Group Subject_term: Qubits;Single photons and quantum effects;Superconducting devices Subject_term_id: qubits;single-photons-and-quantum-effects;superconducting-devices.
- [17] S. Hönl, Y. Popoff, D. Caimi, A. Beccari, T. J. Kippenberg, and P. Seidler, Microwave-to-optical conversion with a gallium phosphide photonic crystal cavity, *Nature Communications* **13**, 2065 (2022).
- [18] W. Jiang, F. M. Mayor, S. Malik, R. Van Laer, T. P. McKenna, R. N. Patel, J. D. Witmer, and A. H. Safavi-Naeini, Optically heralded microwave photon addition, *Nature Physics*, 1 (2023), publisher: Nature Publishing Group.
- [19] M. J. Weaver, P. Duivestijn, A. C. Bernasconi, S. Scharmer, M. Lemang, T. C. v. Thiel, F. Hijazi, B. Hensen, S. Gröblacher, and R. Stockill, An integrated microwave-to-optics interface for scalable quantum computing, *Nature Nanotechnology* **19**, 166 (2024), publisher: Nature Publishing Group.
- [20] S. Meesala, D. Lake, S. Wood, P. Chiappina, C. Zhong, A. D. Beyer, M. D. Shaw, L. Jiang, and O. Painter, Quantum Entanglement between Optical and Microwave Photonic Qubits, *Physical Review X* **14**, 031055 (2024), publisher: American Physical Society.
- [21] H. Zhao, W. D. Chen, A. Kejriwal, and M. Mirhosseini, Quantum-enabled continuous microwave-to-optics frequency conversion (2024), arXiv:2406.02704 [physics, physics:quant-ph].
- [22] L. Fan, C.-L. Zou, R. Cheng, X. Guo, X. Han, Z. Gong, S. Wang, and H. X. Tang, Superconducting cavity electro-optics: A platform for coherent photon conversion between superconducting and photonic circuits, *Science Advances* **4**, eaar4994 (2018).
- [23] T. P. McKenna, J. D. Witmer, R. N. Patel, W. Jiang, R. Van Laer, P. Arrangoiz-Arriola, E. A. Wollack, J. F. Herrmann, and A. H. Safavi-Naeini, Cryogenic microwave-to-optical conversion using a triply resonant lithium-niobate-on-sapphire transducer, *Optica* **7**, 1737 (2020).
- [24] J. Holzgrafe, N. Sinclair, D. Zhu, A. Shams-Ansari, M. Colangelo, Y. Hu, M. Zhang, K. K. Berggren, and M. Lončar, Cavity electro-optics in thin-film lithium niobate for efficient microwave-to-optical transduction, *Optica* **7**, 1714 (2020).
- [25] H. K. Warner, J. Holzgrafe, B. Yankelevich, D. Barton, S. Polletto, C. J. Xin, N. Sinclair, D. Zhu, E. Sete, B. Langley, E. Batson, M. Colangelo, A. Shams-Ansari, G. Joe, K. K. Berggren, L. Jiang, M. Reagor, and M. Loncar, Coherent control of a su-

- perconducting qubit using light (2023), arXiv:2310.16155.
- [26] R. Sahu, W. Hease, A. Rueda, G. Arnold, L. Qiu, and J. M. Fink, Quantum-enabled operation of a microwave-optical interface, *Nature Communications* **13**, 1276 (2022).
- [27] R. Sahu, L. Qiu, W. Hease, G. Arnold, Y. Minoguchi, P. Rabl, and J. M. Fink, Entangling microwaves with light, *Science* **380**, 718 (2023).
- [28] G. Arnold, T. Werner, R. Sahu, L. N. Kapoor, L. Qiu, and J. M. Fink, All-optical single-shot readout of a superconducting qubit (2023), arXiv:2310.16817 [quant-ph].
- [29] M. Shen, J. Xie, Y. Xu, S. Wang, R. Cheng, W. Fu, Y. Zhou, and H. X. Tang, Photonic link from single flux quantum circuits to room temperature (2023), arXiv:2309.03284 [physics, physics:quant-ph].
- [30] W. Fu, M. Xu, X. Liu, C.-L. Zou, C. Zhong, X. Han, M. Shen, Y. Xu, R. Cheng, S. Wang, L. Jiang, and H. X. Tang, Cavity electro-optic circuit for microwave-to-optical conversion in the quantum ground state, *Physical Review A* **103**, 053504 (2021).
- [31] Y. Xu, A. A. Sayem, L. Fan, C.-L. Zou, S. Wang, R. Cheng, W. Fu, L. Yang, M. Xu, and H. X. Tang, Bidirectional interconversion of microwave and light with thin-film lithium niobate, *Nature Communications* **12**, 4453 (2021).
- [32] Y. Xu, W. Fu, Y. Zhou, M. Xu, M. Shen, A. A. Sayem, and H. X. Tang, Light-Induced Dynamic Frequency Shifting of Microwave Photons in a Superconducting Electro-Optic Converter, *Physical Review Applied* **18**, 064045 (2022), publisher: American Physical Society.
- [33] X. Zhu, Y. Hu, S. Lu, H. K. Warner, X. Li, Y. Song, L. Magalhães, A. Shams-Ansari, A. Cordaro, N. Sinclair, and M. Lončar, Twenty-nine million intrinsic Q -factor monolithic microresonators on thin-film lithium niobate, *Photonics Research* **12**, A63 (2024).
- [34] W. Hease, A. Rueda, R. Sahu, M. Wulf, G. Arnold, H. G. Schwefel, and J. M. Fink, Bidirectional Electro-Optic Wavelength Conversion in the Quantum Ground State, *PRX Quantum* **1**, 020315 (2020).
- [35] F. Eltes, G. E. Villarreal-Garcia, D. Caimi, H. Siegwart, A. A. Gentile, A. Hart, P. Stark, G. D. Marshall, M. G. Thompson, J. Barreto, J. Fompeyrine, and S. Abel, An integrated optical modulator operating at cryogenic temperatures, *Nature Materials* **19**, 1164 (2020).
- [36] C. Anderson, G. Scuri, A. White, D. Lukin, E. Szakiel, J. Yang, K. Van Gasse, M. Guidry, W. Jiang, A. Safavi-Naeini, and J. Vuckovic, Quantum critical electro-optic materials for photonics, in *CLEO 2023* (Optica Publishing Group, San Jose, CA, 2023) p. SF1E.5.
- [37] G. A. Smolenskii, N. N. Krainik, N. P. Khuchua, V. V. Zhdanova, and I. E. Mylnikova, The Curie Temperature of LiNbO_3 , *physica status solidi (b)* **13**, 309 (1966).
- [38] M. G. Harwood, P. Popper, and D. F. Rushman, Curie Point of Barium Titanate, *Nature* **160**, 58 (1947).
- [39] S. Abel, F. Eltes, J. E. Ortmann, A. Messner, P. Castera, T. Wagner, D. Urbonas, A. Rosa, A. M. Gutierrez, D. Tulli, P. Ma, B. Baeuerle, A. Josten, W. Heni, D. Caimi, L. Czornomaz, A. A. Demkov, J. Leuthold, P. Sanchis, and J. Fompeyrine, Large Pockels effect in micro- and nanostructured barium titanate integrated on silicon, *Nature Materials* **18**, 42 (2019).
- [40] K. A. Müller and H. Burkard, SrTiO_3 : An intrinsic quantum paraelectric below 4 K, *Physical Review B* **19**, 3593 (1979).
- [41] Y. Fujii and T. Sakudo, Interferometric Determination of the Quadratic Electro-Optic Coefficients in SrTiO_3 Crystal, *Journal of Applied Physics* **41**, 4118 (2003).
- [42] K. D. Fredrickson, V. V. Vogler-Neuling, K. J. Kormondy, D. Caimi, F. Eltes, M. Sousa, J. Fompeyrine, S. Abel, and A. A. Demkov, Strain enhancement of the electro-optical response in BaTiO_3 films integrated on $\text{Si}(001)$, *Physical Review B* **98**, 075136 (2018).
- [43] H. Tian, J. Liu, A. Attanasio, A. Siddharth, T. Blésin, R. Ning Wang, A. Voloshin, G. Lihachev, J. Riemensberger, S. E. Kenning, Y. Tian, T. Han Chang, A. Bancora, V. Snigirev, V. Shadymov, T. J. Kippenberg, and S. A. Bhave, Piezoelectric actuation for integrated photonics, *Advances in Optics and Photonics* **16**, 749 (2024).
- [44] A. K. Hamze, M. Reynaud, J. Geler-Kremer, and A. A. Demkov, Design rules for strong electro-optic materials, *npj Computational Materials* **6**, 130 (2020).
- [45] R. Xu, J. Huang, E. S. Barnard, S. S. Hong, P. Singh, E. K. Wong, T. Jansen, V. Harbola, J. Xiao, B. Y. Wang, S. Crossley, D. Lu, S. Liu, and H. Y. Hwang, Strain-induced room-temperature ferroelectricity in SrTiO_3 membranes, *Nature Communications* **11**, 3141 (2020).
- [46] M. Peruzzo, A. Trioni, F. Hassani, M. Zemlicka, and J. M. Fink, Surpassing the Resistance Quantum with a Geometric Superinductor, *Physical Review Applied* **14**, 044055 (2020).
- [47] R. Barends, H. L. Hortensius, T. Zijlstra, J. J. A. Baselmans, S. J. C. Yates, J. R. Gao, and T. M. Klapwijk, Contribution of dielectrics to frequency and noise of NbTiN superconducting resonators, *Applied Physics Letters* **92**, 223502 (2008).
- [48] K. D. Crowley, R. A. McLellan, A. Dutta, N. Shumiya, A. P. M. Place, X. H. Le, Y. Gang, T. Madhavan, M. P. Bland, R. Chang, N. Khedkar, Y. C. Feng, E. A. Umbarkar, X. Gui, L. V. H. Rodgers, Y. Jia, M. M. Feldman, S. A. Lyon, M. Liu, R. J. Cava, A. A. Houck, and N. P. De Leon, Disentangling Losses in Tantalum Superconducting Circuits, *Physical Review X* **13**, 041005 (2023).
- [49] M. Xu, Y. Wu, W. Dai, and H. X. Tang, Radiatively-cooled quantum microwave amplifiers (2023), arXiv:2308.02106 [quant-ph].
- [50] T. Paoletta and A. A. Demkov, Pockels effect in low-temperature rhombohedral BaTiO_3 , *Physical Review B* **103**, 014303 (2021), publisher: American Physical Society.
- [51] A. Riedhauser and C. Möhl, Absorption loss and Kerr non-linearity in barium titanate waveguides, *APL Photonics* **10**, 10.1063/5.0228990 (2025).
- [52] E. Zeuthen, A. Schliesser, A. S. Sørensen, and J. M. Taylor, Figures of merit for quantum transducers, *Quantum Science and Technology* **5**, 034009 (2020), publisher: IOP Publishing.
- [53] M. Xu, C. Li, Y. Xu, and H. X. Tang, Light-induced microwave noise in superconducting microwave-optical transducers, *Physical Review Applied* **21**, 014022 (2024), publisher: American Physical Society.
- [54] S. Leble, *Practical Electrodynamics with Advanced Applications* (IOP Publishing Ltd, 2020).
- [55] D. F. Walls and G. J. Milburn, *Quantum optics*, 2nd ed. (Springer, Berlin Heidelberg, 2008).
- [56] M. Tsang, Cavity quantum electro-optics, *Physical Review A* **81**, 063837 (2010).
- [57] L. Mandel and E. Wolf, Some general techniques for treating interacting systems, in *Optical Coherence and Quantum Optics* (Cambridge University Press, 1995) 1st ed., pp. 860–899.
- [58] M. Tsang, Cavity quantum electro-optics. II. Input-output relations between traveling optical and microwave fields, *Physical Review A* **84**, 043845 (2011).
- [59] A. P. Gregory, *Q-factor measurement by using a Vector Network Analyser*, Tech. Rep. (National Physical Laboratory, 2022).
- [60] J. Gao, *The Physics of Superconducting Microwave Resonators*, Ph.D. thesis, California Institute of Technology (2008).

[61] J. Rairden and C. Neugebauer, Critical temperature of niobium and tantalum films, *Proceedings of the IEEE* **52**, 1234 (1964).